Nationaal Lucht- en Ruimtevaartlaboratorium
National Aerospace Laboratory NLR

NLR-TP-2003-526

Simulation of limit cycle oscillation of fighter aircraft at moderate angle of attack

B.B. Prananta, J.C. Kok, S.P. Spekreijse, M.H.L. Hounjet and J.J. Meijer

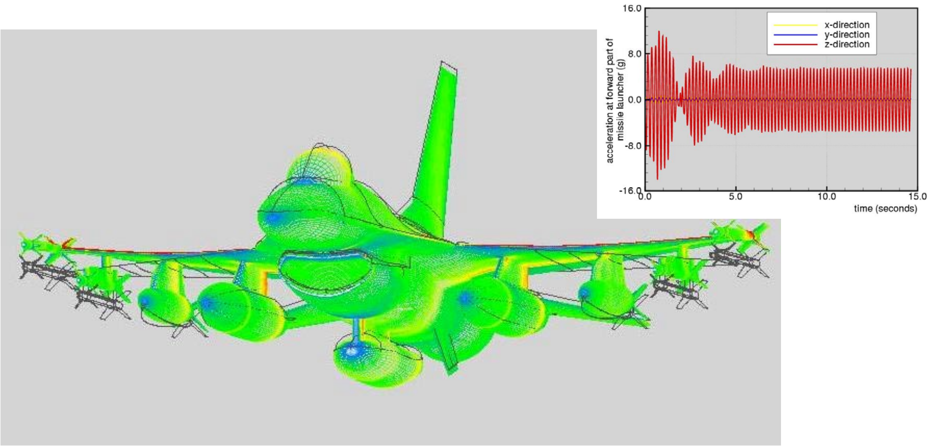

Nationaal Lucht- en Ruimtevaartlaboratorium
National Aerospace Laboratory NLR

NLR-TP-2003-526

Simulation of limit cycle oscillation of fighter aircraft at moderate angle of attack

B.B. Prananta, J.C. Kok, S.P. Spekreijse, M.H.L. Hounjet and J.J. Meijer

This report is based on a presentation held at the International Forum on Aeroelasticity and Structural Dynamics, Amsterdam, The Netherlands, 4-6 June 2003.

This investigation has partly been carried out under a contract awarded by The Netherlands Ministry of Defence monitored by the Royal Netherlands Air Force and as part of NLR's Basic Research Programme. The Netherlands Ministry of Defence and the Royal Netherlands Air Force have granted NLR permission to publish this report.

Working Plan number:	A.1.B.2
Owner:	National Aerospace Laboratory NLR
Division:	Fluid Dynamics
Distribution:	Unlimited
Classification title:	Unclassified
	October 2003

Approved by author:	Approved by project manager:	Approved by project managing department:
BBPr 6/11/2003	6/11/03	5/12/03

Summary

In this paper recent NLR research on transonic limit cycle oscillations of fighter aircraft configurations is reported. Focus is on modelling the dynamic non-linearity of the aerodynamics. Computational aeroelastic simulations of fighter aircraft configurations subjected to complex transonic flow conditions including flow separation are discussed. Important details of the simulation method are highlighted. The simulation method is first applied to standard test cases for limit cycle oscillations due to shock motion (ISOGAI test case) and shock induced flow separation (DLR test case). Finally, the capability of the simulation method to capture limit cycle oscillations of an F-16 aircraft in heavy store configuration and at moderate angles of attack in transonic flow is demonstrated. The obtained results confirm the role of shock-induced flow separations as one of the possible causes of limit cycle oscillations for specific fighter aircraft configurations.

Contents

(38 pages in total)

SIMULATION OF LIMIT CYCLE OSCILLATION OF FIGHTER AIRCRAFT AT MODERATE ANGLE OF ATTACK *

B.B. Prananta[1], J.C. Kok[2], S.P. Spekreijse[3], M.H.L. Hounjet[4]
and J.J. Meijer[5]

[1,2,4,5]National Aerospace Laboratory NLR
Anthony Fokkerweg 2, 1059 CM Amsterdam, The Netherlands
`e-mail:` [1]`prant@nlr.nl` [2]`jkok@nlr.nl` [4]`hounjet@nlr.nl` [5]`meijer@nlr.nl`

[3] National Aerospace Laboratory NLR
Voorsterweg 31, 8316 PR Marknesse, The Netherlands
`e-mail:` [3]`sspek@nlr.nl`

Keyword: aeroelasticity, computational fluid dynamics, Navier-Stokes equations, limit cycle oscillation, flutter

Abstract. In this paper recent NLR research on transonic limit cycle oscillations of fighter aircraft configurations is reported. Focus is on modelling the dynamic non-linearity of the aerodynamics. Computational aeroelastic simulations of fighter aircraft configurations subjected to complex transonic flow conditions including flow separation are discussed. Important details of the simulation method are highlighted. The simulation method is first applied to standard test cases for limit cycle oscillations due to shock motion (ISOGAI test case) and shock induced flow separation (DLR test case). Finally, the capability of the simulation method to capture limit cycle oscillations of an F-16 aircraft in heavy store configuration and at moderate angles of attack in transonic flow is demonstrated. The obtained results confirm the role of shock-induced flow separations as one of the possible causes of limit cycle oscillations for specific fighter aircraft configurations.

1 INTRODUCTION

It is well-known that several types of modern fighter aircraft suffer from sustained vibrations known as the limit cycle oscillation or LCO. A large number of investigations have been, and are, devoted to this topic to investigate the cause of the problem. However, until now a comprehensive insight into the problem has not been reached. This type of vibrations hampers the effective use of these aircraft, mostly when carrying different types of stores. For instance, the Royal Netherlands Air Force (RNLAF) operates F-16 fighter aircraft which are susceptible to limit cycle oscillation for certain heavy store configurations. Investigation of limit cycle oscillations is important in association with operational limits, safety aspects and also the influence on maintenance aspects such as fatigue. The repeating loads during LCO may have some influence on the life cycle consumption.

It is generally accepted that non-linearity in the aeroelastic system plays an essential role in limit cycle oscillation phenomena. For a complex aeroelastic system such as a fighter aircraft the

---

*The work presented in this paper is partly funded by the Netherlands Ministry of Defence through the AESIM-MIL project contract number (NTP) N98/04.

nonlinearity may originate from various sources, e.g. structural nonlinearity (stiffness, damping, free-play), aerodynamic nonlinearity (shock-induced flow separation, shock wave motion, vortex dynamics), control-system nonlinearities, etc.

Several LCO investigations published in the literature have been directed towards modelling of structural nonlinearity, e.g. Refs. [2, 15] on the nonlinear damping and Ref. [21] on the stiffness nonlinearity. NLR in co-operation with Lockheed Martin Aeronautics has been exploring nonlinearities in the aerodynamics. Various wind-tunnel campaign have been carried out, both steady and unsteady, to characterise the transonic flow about the F-16 fighter aircraft during limit cycle oscillation. Semi-empirical models are then co-developed based on the measured data and have been successfully applied, e.g.[13, 14], to model limit cycle oscillations at moderate angles of attack where shock-induced flow separation occurs. Further applications of the method, however, are hampered by the availability of the required data. New approach is therefore necessary either to generate high fidelity aeroelastic database or to be applied directly to simulate and analyse LCO phenomena.

In the past years, a computational aeroelastic simulation system has been developed at NLR. The system embodies a suitable platform for investigating non-linearities in the aeroelastic system. Based on the experience at hand, a first step is taken in which a linear structural model is used along with a nonlinear flow model based on the Euler/Navier-Stokes equations. In the following sections the methods underlying the computational aeroelastic simulation system and its validation will be presented in detail.

Results of dynamic aeroelastic simulation for standard test cases are shown first. The applicability of the method is finally demonstrated by simulating limit cycle oscillation of an F-16 fighter aircraft in transonic flow at a moderate angle of attack. The predicted frequency of the limit cycle oscillation is comparable to with the results of flight measurement.

2 AEROELASTIC SYSTEM

The aeroelastic simulation system that has been developed at the NLR in the past years is based on the NLR CFD tool, i.e. the ENFLOW system. The ENFLOW CFD system consists of the ENDOMO domain modeller, the ENGRID grid generator, the ENSOLV flow solver and the ENADAP grid adaptation tool. The flow model employs the Euler/Reynolds-Averaged Navier-Stokes equations while the geometry modelling uses structured multiblock grids. The ENFLOW system is the workhorse at NLR for activities requiring high fidelity flow simulations such as aerodynamic performance prediction, aircraft-engine integration, support for wind tunnel measurement, unsteady cavity flow, unsteady flow about oscillating wing, internal flow inside aircraft cabin, etc.

The extension of the ENFLOW system as a computational aeroelastic simulation (CAS) system has been driven by the need to investigate various aeroelastic phenomena associated with complex flows that commonly occur about military aircraft configurations, e.g. shock waves, vortex flow, shock-induced flow separation, etc. The ENFLOW CAS system can be applied for static aeroelastic simulation on a routine basis, e.g. Refs. [19, 25]. However, dynamic aeroelastic simulations using the ENFLOW CAS system are mostly carried out for specific investigations and seldom for routine applications. This situation is expected to change in the near future. The NLR aeroelastic tool that is designed for routine industrial applications is called the AESIM-BASIC system. The NLR AESIM-BASIC system is based on the linear lifting surface and the non-linear full potential aerodynamic model.

The equations governing the mechanics of an aeroelastic system consist of the equations governing the dynamics of the structure of the aircraft and the equations governing the flow field around the aircraft. The deformation of the structure is assumed to be relatively small, therefore a linearised structural model is employed. The nonlinear Euler/Navier-Stokes equations are used to model the flow field around the aircraft. In a non-dimensional form the set of governing equations can be written as:

$$\begin{aligned} \boldsymbol{M}\ddot{\boldsymbol{x}} + \boldsymbol{C}\dot{\boldsymbol{x}} + \boldsymbol{K}\boldsymbol{x} &= \frac{1}{2} V^{*2}\, \boldsymbol{C}_A(Q, \boldsymbol{x}, \dot{\boldsymbol{x}}, t), && (1) \\ \frac{\partial Q}{\partial t} + \boldsymbol{\nabla} \cdot \mathcal{F}(Q, \dot{\boldsymbol{x}}; Re_\infty, M_\infty) &= \mathcal{S}(Q, \dot{\boldsymbol{x}}; Re_\infty, M_\infty). && (2) \end{aligned}$$

These equations are coupled through the kinematic condition at the fluid/structure interface. Let $\boldsymbol{n}$ be a vector normal to the fluid/structure interface. The kinematic boundary condition for the flow field on the solid surface of the configuration then becomes:

$$\begin{aligned} (\boldsymbol{u} - \dot{\boldsymbol{x}}) \cdot \boldsymbol{n}(\boldsymbol{x}) &= 0, \quad \text{for inviscid flow;} && (3) \\ \boldsymbol{u} - \dot{\boldsymbol{x}} &= 0, \quad \text{for viscous flow.} && (4) \end{aligned}$$

This boundary condition is completed by conditions for the thermodynamic quantities, e.g. the adiabatic wall condition. In equations (1) to (4), $\boldsymbol{M}$ is the mass matrix, $\boldsymbol{C}$ is the damping matrix, $\boldsymbol{K}$ is the stiffness matrix and $\boldsymbol{C}_A$ is the aerodynamic force coefficient vector which is a function of the flow state vector $Q = [\rho, \rho\boldsymbol{u}, \rho E, \rho T^1, .., \rho T^{N_T}]^T$ where ρ is the density, $\boldsymbol{u} = [u, v, w]^T$ is the velocity vector, E is the total energy per unit mass, and $T^1, .., T^{N_T}$ are the variables for the turbulence models. $\mathcal{F}$ and $\mathcal{S}$ are the flux matrix and the source term in the Euler/Navier-Stokes equations, respectively.

In addition to the usual similarity parameters, i.e. the Reynolds number Re_∞, the Mach number M_∞, and the coefficient of aerodynamic force $\boldsymbol{C}_A$, a fluid/structure interaction parameter, the so-called speed index V^*, is involved in the governing equations. V^* is defined as:

$$V^* = \frac{U_\mathsf{R}}{\sqrt{\mu}}, \tag{5}$$

where $U_\mathsf{R} = u_\infty/(\omega_\mathsf{ref} L_\mathsf{ref})$ and $\mu = m_\mathsf{ref}/(\rho_\infty v_\mathsf{ref})$ are the reduced velocity and the mass ratio, respectively. U_R and μ are defined by the reference frequency ω_ref, the reference mass m_ref, the reference volume v_ref, the reference length L_ref, the free-stream velocity u_∞, and the free-stream density ρ_∞. The mass ratio is a parameter representing the ratio of the reference mass (mass of the structure) and the mass of the surrounding air. In the present formulation, the reference volume is defined as v_ref=L^3_ref. All similarity parameters are invariant across the fluid/structure interface.

To take the advantage of the available methods for the aerodynamics and structural dynamics a loosely coupled method is adopted. Such method is built upon three distinct components: (i) unsteady aerodynamic part, (ii) structural dynamic part and (iii) space and time synchronisation. In the following sections some aspects of these components are discussed.

2.1 Unsteady aerodynamics

The Euler/Reynolds-Averaged Navier-Stokes equations are discretised following a cell-centred finite-volume method in multiblock structured grids. Second-order central differencing with either scalar of matrix numerical dissipation is adopted. Time-accurate integration is carried out using a dual-time stepping scheme:

$$\frac{dQ^{n+1}}{dt_{\mathsf{P}}} + R(Q^{n+1}; Q^n, Q^{n-1}) = 0, \tag{6}$$

with the Runge-Kutta method for the relaxation in the pseudo time t_{P}. The residual $R(Q^{n+1}; Q^n,$ $Q^{n-1})$ includes the time derivative of the flow state Q, approximated using second order backward differences. Convergence acceleration is provided by FAS multigrid method and a line-relaxation method.

When the method is applied to simulate turbulent flows, Reynolds averaging is used and an additional model is required to represent the Reynolds stresses. Several turbulence models are available in ENSOLV including algebraic models and various variants of the $k - \omega$ two-equation turbulence model. In the present work, all viscous computations have been carried out using the NLR TNT (turbulent-non-turbulent) $k - \omega$ turbulence model. The TNT variant of $k - \omega$ turbulence model removes the unnecessary dependency of the results on the free-stream turbulence level [10]. Another important aspect of the turbulence model is the ability to handle strong shock-boundary layer interaction. For this purpose, the explicit algebraic Reynolds stress model has been augmented to the present NLR TNT $k - \omega$ turbulence model.

During an aeroelastic simulation, the multiblock grids have to deform to follow the deformation of the fluid/structure interface due to the aerodynamic and inertial loads. In the present work, a robust and efficient grid deformation technique has been developed. The method combines a three-dimensional spline technique, e.g. the volume spline of Ref. [8], and a standard transfinite interpolation technique. The first is applied to the block boundaries while the second is applied to the grid inside the block. A more detailed description can be found in Ref. [22].

2.2 Structural dynamics

To take advantage of the fact that dynamic aeroelasticity of aircraft concerns mainly low frequency vibrations, a modal approach is applied. The structural deformation is mapped to a preselected vector space with a limited number of degrees of freedom:

$$\boldsymbol{h}(t) \approx \boldsymbol{\phi}_1 q_1(t) + \boldsymbol{\phi}_2 q_2(t) + ... + \boldsymbol{\phi}_N q_N(t) = [\boldsymbol{\phi}]\{q(t)\}, \tag{7}$$

where $\boldsymbol{h}$ is the deformation of the structure and q_i is called a generalised coordinate. The modal space $[\boldsymbol{\phi}]$ is selected to be the eigenvectors of the system of undamped structural dynamic equations, also called the mode shapes of the structure. In most cases, the required number of mode shapes involved in the analysis, N, is much smaller than the number of degrees of freedom of the model to represent the dynamics of the structure.

Due to orthogonality of the mode shapes with respect to the mass and stiffness matrices, inserting equation (7) into equation (1) results in a set of equations:

$$m_i \ddot{q}_i + 2\zeta_i m_i \omega_i \dot{q}_i + m_i \omega_i^2 q_i = Q_i, \qquad i = 1...N, \tag{8}$$

where $m_i = \phi_i^T\, \boldsymbol{M}\, \phi_i$ is the generalised mass with $\boldsymbol{M}$ the mass matrix, ζ_i is the modal damping coefficient, and ω_i is the natural frequency. $Q_i = \boldsymbol{\phi}_i \cdot \boldsymbol{F}_{\mathsf{srf}}$ is the generalised aerodynamic force (GAF) where $\boldsymbol{F}_{\mathsf{srf}}$ is the surface force vector due to the pressure and viscous forces. In equation

(8), the damping matrix has been assumed to be proportional to the mass and stiffness matrices. Equations (8) are coupled by the generalised aerodynamic forces, Q_i.

The second order ordinary differential equation (ODE), equation (8), is integrated in time using the transition matrix method after a transformation into a set of first order ODE's. This technique is commonly applied in flight mechanics problems but proves to be also very useful for aeroelastic problems, see Refs. [4, 16, 18].

The required structural data for the simulations, i.e. the mode shape, the generalised mass and the generalised stiffness, have been obtained in the present work with the help of finite element method. The NASTRAN finite element package has been used to generate the modal data for the three-dimensional cases considered in the present paper, i.e. the AGARD 445.6 wing and the F-16 heavy store configuration. The overview of the finite element model for the AGARD 445.6 wing is shown in Figure 3 and the model for the F-16 heavy store configuration is shown in Figure 4.

2.3 Fluid/structure synchronisation

As consequence of adopting a loosely coupled scheme a synchronisation in space and time between the aerodynamic part and the structural part has to be devised.

The modelling of the fluid/structure interface according to requirements set in the aerodynamic part and in the structural part is in most cases different. This implies that an interpolation is needed to interchange the interface data, i.e. the deformation and the loads. Here, a spline method is used which interpolates the deformation of the fluid/structure interface computed in the structural part. Various types of spline methods can be applied according to the available data, i.e. surface spline, volume spline, component-wise spline, etc., see Ref. [8] for a comprehensive description of spline methods for aeroelastic applications.

time level	aerodynamic module		structural module
n	$\boldsymbol{U}^{n+\frac{1}{2}} \approx \mathcal{P}(\boldsymbol{X}^{n-1}, \boldsymbol{X}^{n-2}..., \boldsymbol{U}^{n-1}, \boldsymbol{U}^{n-2}...)$	$\rightarrow$	receive $\boldsymbol{U}^{n+\frac{1}{2}}$
	receive $\boldsymbol{X}^{n+1}$	$\leftarrow$	$\boldsymbol{X}^{n+1} = \Phi \boldsymbol{X}^n + \Theta \boldsymbol{U}^{n+\frac{1}{2}} \quad (*)$
	deform aerodynamic grid		
	solve $R(Q^{n+1}; Q^n, Q^{n-1}) = 0$		
	$\boldsymbol{U}^{n+\frac{1}{2}} = \frac{1}{2}(\boldsymbol{U}^n + \boldsymbol{U}^{n+1})$	$\rightarrow$	receive $\boldsymbol{U}^{n+\frac{1}{2}}$
			`if` required back to $(*)$
$n+1$			`else` time level $n+1$ is reached

Table 1: Aero-structural iteration scheme for the simultaneous time integration of the aeroelastic equations

Time integration of an aeroelastic system presents a special problem due to the interdependency of the subsystems, i.e. the structural part and aerodynamic part. Solving the aerodynamic equations requires the deformation of the surface computed in the structural part while the structural equations of motion can only be solved when the aerodynamic forces are available. In the present work, an iterative scheme is used in each time step which leads to a fully-implicit convergence of the whole aeroelastic system. In such approach the following items have been found important to ensure good convergence of the fluid/structure iteration:

- Proper initial condition, i.e. prediction of the state at the next time step, for the aerodynamic part and structural part.
- Prior to interchanging the data, sufficient convergence should be obtained, i.e. the data should be sufficiently smooth.

Concerning the initial condition, two possibilities can be followed: predicting the aerodynamic forces at the next time step and solving the structural deformation or predicting the structural deformation at the next time step and solving the aerodynamic equations. The first scheme, called aerodynamic extrapolation method, is applied in ENSOLV. Experience with the aeroelastic system up to now shows that the aerodynamic extrapolation scheme yields satisfactory results and requires only a very small number of iterations in each time step to obtain convergence. The aerodynamic extrapolation method is summarised in Table 1 where the sequence or processes during one step from time level (n) to time level $(n+1)$ is shown. The predictor $\mathcal{P}$ in Table 1 can be a simple extrapolation method, e.g. Refs. [4, 17], or an advanced prognostic method involving parameter identification technique, e.g. Ref. [7, 17].

2.4 Special case, two-dimensional model

For two-dimensional cases, the standard procedure to reduce the number of degree of freedom by applying the modal approach as described in previous section, is not performed because this case features only two degrees of freedom. For the sake of completeness the simplification of the aeroelastic system that is applicable to a two-dimensional aerofoil is presented in this section.

The equations of motion for a typical wing section can be derived by balancing the forces and moments around the elastic axis EA, see Figure 2. Assuming small structural deformations, the equations of motion become:

$$\begin{bmatrix} 1 & -x_\alpha \\ -x_\alpha & r_\alpha^2 \end{bmatrix} \begin{Bmatrix} \ddot{h} \\ \ddot{\alpha} \end{Bmatrix} + 2 \begin{bmatrix} \delta_h \bar{\omega} & 0 \\ 0 & \delta_\alpha r_\alpha^2 \end{bmatrix} \begin{Bmatrix} \dot{h} \\ \dot{\alpha} \end{Bmatrix} + \begin{bmatrix} \bar{\omega}^2 & 0 \\ 0 & r_\alpha^2 \end{bmatrix} \begin{Bmatrix} h \\ \alpha \end{Bmatrix} = \frac{1}{2} V^{*2} \begin{Bmatrix} C_L \\ C_M \end{Bmatrix}, \qquad (9)$$

where the chord length c has been used as the reference length, mass of the aerofoil per unit span m as the reference mass and the uncoupled natural frequency of the rotation motion $\omega_\alpha = \sqrt{K_\alpha / I_\alpha}$ as the reference frequency with K_α the stiffness of the rotational spring and I_α the moment of inertia about the elastic axis EA. In equation (9) h is the translational displacement (positive upwards), x_α is the distance between elastic axis EA and the centre of gravity CG, α is the angle of attack, $\bar{\omega} = \omega_h / \omega_\alpha$ is the ratio of uncoupled natural frequencies, δ_h is the damping coefficient for translational motion, δ_α is the damping coefficient for the rotation motion and $r_\alpha = \sqrt{4 I_\alpha / (m c^2)}$ is the dimensionless radius of gyration with respect to EA.

In this paper two two-dimensional cases will be presented, i.e. the ISOGAI case of NACA 64A010, Refs.[9] and the DLR case of NLR 7301, Ref. [20]. The values of the parameters for these cases are presented in Table 2. The values for the ISOGAI case are representative for a swept-back wing, i.e. the elastic axis EA is located in front of the leading edge of the section and the frequency ratio of the first mode (bending) and the second mode (torsional) is relatively high.

For a simplified wind-on analysis, the steady aerodynamics model for a flat plate in incompressible flow can be used. In this case, the aerodynamic lift force and pitching moment depend only

parameter	ISOGAI case	DLR case	remark
aerofoil	NACA 64A010	NLR 7301	
a	-0.50	0.25	position of EA measured from the nose
x_α	0.90	0.0484	
r_α^2	3.48	0.3881	
ω_h/ω_α	1.0	0.761	
ω_1/ω_α	0.713	0.735	first coupled natural frequency
ω_2/ω_α	5.338	1.070	second coupled natural frequency

Table 2: Aeroelastic parameters of a characteristic aerofoil suitable for two-dimensional aeroelastic modelling

on the angle of attack. The dynamic angle of attack formulation is used in which the effect of the plunging motion is included in the pitching motion through the dynamic angle of attack:

$$\alpha_{\mathsf{dyn}} = \alpha + \frac{\dot{h}}{u_\infty}. \tag{10}$$

The coefficients of the lift force and pitching moment around the elastic axis can then be expressed as:

$$\begin{Bmatrix} C_L \\ C_M \end{Bmatrix} \approx \begin{Bmatrix} C_{L_0} \\ C_{M_0} \end{Bmatrix} + \begin{bmatrix} 0 & C_{L\alpha} \\ 0 & -eC_{L\alpha} \end{bmatrix} \begin{Bmatrix} h \\ \alpha \end{Bmatrix} + \begin{bmatrix} -C_{L\alpha}/u_\infty & 0 \\ eC_{L\alpha}/u_\infty & 0 \end{bmatrix} \begin{Bmatrix} \dot{h} \\ \dot{\alpha} \end{Bmatrix} \tag{11}$$

where the value of the gradient with relation to angle of attack of the lift coefficient is taken to be $C_{L\alpha} = 2\pi$ and e is the distance between elastic axis and aerodynamic centre.

3 RESULTS OF SIMULATIONS

The results of the dynamic aeroelastic simulations using the newly developed CAS system based on the NLR ENFLOW CFD system are now presented. First, standard test cases are simulated to validate the CAS method.

3.1 Fluid/structure iteration procedure

As mentioned in the previous section, an iteration procedure is applied to drive a fully-implicit convergence of the aeroelastic system. Dynamic aeroelastic simulations have been carried out to check the present fluid/structure iteration procedure. To isolate this issue, a simplified aeroelastic system is used in the first set of computations, i.e. a two-dimensional aerofoil approximated by a flat plate. Furthermore, steady aerodynamic theory for incompressible flow is used instead of the full solution obtained from the CFD module, see equation (11) in section 2.4. The simple expressions for the aerodynamic forces and pitching moment allow an implicit treatment of them in the time integration scheme, i.e. this results into implicit integration for the whole aeroelastic system. Furthermore, since an analytical expression for the transfer matrix method is used, the solution is exact. Aeroelastic parameters studied by Zwaan [28] are used in the present investigation, i.e. $\mu = 100$ and $e = -0.50$ chord. The flutter speed expressed in terms of the reduced velocity $U_{\mathsf{R}} = u_\infty/(\omega_\alpha b)$ is given in Ref. [28] to be about 20. Simulations have been carried out with a small initial velocity at $t = 0$ as initial condition for stable condition at $U_{\mathsf{R}} = 18$, neutral condition at $U_{\mathsf{R}} = 20$ and unstable condition at $U_{\mathsf{R}} = 21$. The results are shown in Figure 5. Next, the dynamic aeroelastic simulation at $U_{\mathsf{R}} = 18$ is repeated using the loosely-coupled fluid/structure coupling method. Three simulations have been carried out with different numbers of structural updates. The results, depicted in Figure 6, show that only the response with one structural update differs from the other responses, including the exact solution. Thus convergence is obtained using a small number of updates.

To check whether a similar conclusion can be drawn for simulations involving nonlinear aerodynamics, the CFD module of the ENFLOW system is used for aerodynamic computations based on the Euler equations on the NACA 64A010 aerofoil at the transonic condition of $M_\infty = 0.85$ and $U_\mathsf{R} = 4.26$. Three multigrid cycles have been carried out before the structural position is updated. Figure 7 presents the results of the simulations in terms of the responses for the pitching and plunging motions. The results for one, two and three structural updates in the fluid/structure coupling procedure are hardly distinguishable. Looking closely to a peak of the responses, a similar observation can be made as for the flat plate case in the sense that responses obtained with two and three structural updates almost coincide.

Based on the results presented in this section, it is concluded that the present loosely-coupled scheme is efficient and robust. Only a small number of fluid/structure iterations is required per time step to obtain sufficient convergence of the aeroelastic system.

3.2 Flutter of the AGARD standard test case: 445.6 wing

The results of the computations on the standard three-dimensional dynamic aeroelastic test case of AGARD are presented in this section. The case of weakened wing 445.6 number 3 is selected. The purpose of the investigation is to establish the applicability of the present CAS method for transonic flutter simulation.

Following the suggestion given in Ref. [27], the first four mode shapes of the 445.6 wing have been used in the simulation along with the measured natural frequencies. The mode shapes in the nodes of the structural grid and the interpolated ones on the aerodynamic grid are shown in Figure 8. The contours on the grids correspond to associated magnitudes of the mode shape which is in this case only the deformation in the z-direction. Since the data is completely located on a two-dimensional surface, the surface spline method has been used to interpolate the mode shapes.

The aeroelastic simulations have been started with the computation of the steady flow field based on the Euler equations around the wing at zero angle of attack. Next, the required response is generated by application of the initial condition of a relatively small generalised velocity for all mode shapes at $t = 0$. In order to determine a suitable size of the time step, two simulations at $M_\infty = 0.96$ and speed index $V^* = u_\infty/(\omega_2 c_\mathsf{R}\sqrt{\mu}) = 0.2$ have been carried out. The time step size is determined with respect to the highest natural frequency of the mode shapes involved in the simulation. The duration of the simulation is defined by the required number of periods of the lowest natural frequency of the mode shapes. Figure 9 shows the time history of the generalised coordinates of the second and third mode shapes obtained from simulations using time step sizes $\Delta t = T_4/8$ and $\Delta t = T_4/16$, respectively. Up to four periods of the first mode shape are simulated to obtain enough samples. It is clear from the figure that only small differences exist between the two generalised coordinates which suggests that the time step is sufficiently small to properly model the system. To be on the safe side, all computations described in the remainder of the present paper have been carried out with 16 samples of the highest structural natural frequency involved in the simulation.

The flutter boundary has been predicted through the execution of simulations at several speed-indices, approximation of the damping for each simulation and interpolation to obtain a speed index associated with zero damping. In the present study, the damping for each simulation is approximated simply using a logarithmic decrement technique. More advanced methods can also be applied, e.g. [7]. Note that post-processing of time-domain simulation results deserves significant attention and is beyond the scope of the present work. In a logarithmic decrement technique, the damping of the system is assumed to be proportional to the logarithm of the ratio of two consecutive peaks in the response. In each simulation, the average of the damping for several consecutive peaks is used. Figures 10 and 11 show two examples of the responses of the first and second mode shapes of the 445.6 wing at subsonic ($M_\infty = 0.499$) and supersonic ($M_\infty = 1.114$) flow, respectively. At each Mach number, stable and unstable responses have been obtained.

Comparison of the flutter boundaries obtained from four computational methods and experimental data of NASA [27] is presented in Figure 12. The computational results are obtained from ENFLOW with flow model based on the Euler equations, from Lee-Rausch and Batina [11] also based on the Euler equations on structured grids, from Farhat and Lesoinne [5] based on the Euler equations on unstructured grids, and from Hounjet and Eussen [6] based on the full potential equation. This figure shows that the flutter boundary is lowest in terms of the speed index at a free-stream Mach number close to unity. This property is known as the transonic dip. Further inspection shows that at subsonic speed, all Euler results correspond well, and also correspond well to the experimental data of NASA. The flutter boundary computed using the full potential method is somewhat higher in terms of speed index than those obtained using the Euler methods. At supersonic speed, however, the flutter boundary obtained by Farhat and Lesoinne [5], diverges from the other Euler results but corresponds well to the experimental boundary. The flutter boundaries predicted using ENFLOW and CFL3D of NASA [11], correspond mutually well at these speeds, but yield a considerably higher flutter boundary than the experimental boundary. It is suggested in Ref. [11] that at this supersonic speed the effect of viscosity is significant which may explain this difference. The results in Ref. [5], also obtained from computations based on the Euler equations for inviscid flow, have been obtained using a very coarse unstructured grid. The associated substantial numerical dissipation seems to have a favourable effect by mimicking real viscosity.

Based on the presented results of dynamic aeroelastic simulations for the AGARD 445.6 wing, it may be concluded that, at least for attached flow fields, the present CAS method has been validated for transonic flutter simulations.

3.3 Flutter and inviscid LCO of the NACA-64A010 aerofoil

The interesting LCO case of the NACA 64A010 aerofoil in transonic flow is considered. This case shows important features of transonic aeroelastic phenomena: a pronounced transonic dip, multiple flutter boundary and LCO. The aeroelastic parameters of Isogai [9] as given in Table 2 are used in the present simulations. Although experimental data for this case is not available, many computational results have been published in the literature and can be used for comparison.

The flutter boundary is predicted in a similar manner as in the case of AGARD wing through simulations at various speed indices, defined as $V^* = u_\infty/(\omega_\alpha b\sqrt{\mu}$, approximating of the damping of the responses and interpolation to obtain a speed index associated with zero damping. Logarithmic decrement technique is also applied to approximate the damping for each simulation. Figure 13 shows the flutter boundaries obtained using the ENFLOW system based on the Euler equations and those available in the literature, i.e. results employing the Euler equations from Bendiksen and Kousen [1] and Darracq et al. [3] (CERFACS), results using the full potential equation from Hounjet and Eussen [6] and results using the linear doublet lattice method. This figure clearly shows the inadequacy of the linear doublet lattice method to produce a conservative prediction of the flutter speed at transonic conditions. The flutter boundary computed using ENFLOW corresponds well to the CERFACS results. The results from Bendiksen and Kousen [1], that are the first published results using the Euler equations for this case, have been obtained from computations on a relatively coarse grid which explains the differences with the two other Euler results. One of the features of the present NACA 64A010 aerofoil test case is the existence of multiple flutter boundaries at a range of Mach numbers. Figure 13 shows that between $M_\infty = 0.85$ and 0.90 a stable region exists above the (first) flutter boundary. This stable region is bounded by a second flutter boundary at speeds higher than the speeds associated with the first boundary.

Next, conditions beyond the first flutter boundary are investigated at $M_\infty = 0.875$. Figure 14 shows the time histories of plunging and pitching motions at three speed indices beyond the first flutter boundary. It can be seen in the figure that the amplitudes of the oscillations increase to a relatively large value and thereafter the amplitudes of responses remain at a constant level. This type of response is identified as the limit cycle oscillation LCO. The figure shows also that the magnitudes of the limit cycle oscillation amplitudes depend on the speed index. However, the final state of the LCO does not depend on the initial condition. This is in contrast to the results obtained from linear systems that depend on the initial conditions. Figure 15 shows the phase plane, i.e. the plot showing the relation between displacement and velocity, for the pitching motion at speed index $V^* = 0.60$ and for two initial conditions. The first simulation is started using a relatively small initial velocity and the second using a relatively large velocity. The responses follow different paths but eventually arrive at the same LCO state.

The dependency of the LCO amplitude on the speed index is clearly shown in Figure 16. Stable responses are represented by zero LCO amplitudes. After the first flutter boundary is crossed, the response exhibits LCO whose amplitude increases initially with the increase of the speed index. However, for even higher speed indices the amplitude of LCO decreases again until a stable response (zero LCO amplitude) is reached. After the second flutter boundary is crossed, LCO responses are obtained again, but with larger amplitudes compared to the previous area with LCO responses. The first LCO constitutes a bending-torsion mode and the second LCO a dominantly torsion mode. Similar results for LCO have also been reported in the literature, e.g. Refs. [1]. It is worth noting that the amplitude of the first LCO features an apparent discontinuity at its inception at $V^* \approx 0.60$, while it terminates continuously at $V^* \approx 1.8$. This discontinuous inception of the LCO is indicative of the possibility of the existence of unstable LCO as in the case of aileron buzz, see Steger and Bailey [23]. The present numerical approach is not suitable to capture an unstable LCO. However, this is not an undesirable property of the method, since unstable LCO is in practice not of importance.

3.4 LCO of the NLR-7301 aerofoil

The other interesting LCO case based on a relatively recent measurement campaign is the DLR case of NLR 7301 aerofoil, see e.g. Schewe et al. [20]. Flutter boundary and the condition beyond the flutter margin were investigated during the wind-tunnel measurement. Due to the increasing interest in the LCO phenomena in the past years, this test case became one of the most important validation cases for transonic flutter and LCO. Several computational results have been published in literature, e.g. Tang et al. [24], Weber et al. [26], and there is no doubt that many others will follow.

The DLR case is a two-dimensional two-degree-of-freedom, in pitch and plunge, aeroelastic system subjected to transonic flow condition. The experimental set up does not include structural nonlinearities. The theoretical model of DLR experiment is similar to the ISOGAI case except that it contains viscous damping parameters. The structural data of the DLR case is given in Table 2. As suggested in Ref. [20], the measuring point number 77 (MP77) is selected. The free-stream Mach number is $M_\infty = 0.768$, mean angle of attack $\alpha = 1.28$, Reynolds number $Re_\infty = 1.727$ million based on the chord length, mass ratio $\mu = m_{\mathsf{ref}}/(\rho_\infty \pi b^2 s) = 954.0$ and speed index $V^* = u_\infty/(\omega_\alpha b\sqrt{\mu}) = 0.204$, where b is the half chord and s is the span of the wing. MP77 represents condition beyond flutter boundary close to the bottom of the transonic dip. A two-degree of freedom transonic LCO is observed during the experiment.

Due to the significant size of the model compared to the wind tunnel test section, correction should be applied to the measurement condition, i.e. the Mach number and angle of attack. Weber et al. [26] also found that modelling of the porous wall of the wind-tunnel could influence the results significantly. In the present paper, no attempt has been made to investigate this correction, the correction as suggested in [20] has been used. Future research will take this matter into account.

Aeroelastic simulations have been carried out at $M_\infty = 0.754$ and $\alpha = -0.15$ degree using flow model based on the Reynolds-Average Navier-Stokes equations. The TNT $k - \omega$ turbulence model augmented with explicit algebraic Reynolds stress model. An initial condition in the form of velocity at $t = 0$ is applied. The results in terms of the history of plunging and pitching deformation and velocity are shown in Figure 17 and Figure 18. Results for two initial conditions have been shown in these figures, i.e. small and large disturbance. Contrary to the observation of Tang et al. [24] where the final LCO state depends on the magnitude of the disturbance, here similar final LCO states are reached for both simulations with small and large disturbance initial condition. In other word, in the present simulations only one LCO state has been found. Further investigation of this test case will be carried out including careful parameter study to investigate the existence of multiple LCO states as found by Tang et al. [24].

methods	α_{LCO} (degree)	h_{LCO}/c	$\omega_{\mathsf{LCO}}/\omega_\alpha$	ϕ_{LCO} (degree)
present method	5.04	0.050	0.775	169.9
Tang et al. [24]	3.17	0.030	0.793	n.a.
Weber et al. [26]	4.09	0.035	0.772	169.8
experiment [20]	0.18	0.002	0.759	176.7

Table 3: Comparison of several LCO parameters between computational results and experiment for the DLR case of NLR 7301 aerofoil at condition MP77, $M_{\infty\mathsf{EXP}} = 0.768$, $\alpha_{\mathsf{EXP}} = 1.28$ degree

The comparison of some LCO parameters with other computational results and the experiment is presented in Table 3. Similar to the other computational results, the amplitude of the LCO is far larger than that measured in the experiment. As mentioned before a porous wall modelling can influence the results significantly [26]. In the present computations a free-stream boundary has been used. However, the good agreement of the frequency $\omega_{\text{LCO}}/\omega_\alpha$ and the phase-lag between pitching motion and plunging motion ϕ_{LCO} at LCO condition suggests that the LCO mechanism has been modelled properly by numerical simulations.

3.5 LCO of the F-16 aircraft heavy store loading configuration

The final test case considered in this paper is the F-16 aircraft in an air-to-ground heavy store loading configuration. The purpose of this test case is not to analyse extensively the aeroelastic characteristics of the F-16 because such activities are beyond the scope of the present paper. Instead, it is intended to demonstrate the capability of the present CAS method to model LCO of a real fighter aircraft configuration. The air-to-ground configuration considered here is shown in Figure 19 (the upper left figure). From a geometry point of view, the configuration is extremely complex, i.e. including AIM-9J missiles mounted at the tip of the wing and at the outboard underwing attachment, a MK-84 bomb mounted at the mid underwing attachment, and a full 370-GALLON fuel tank mounted at the inboard underwing attachment. This configuration is also known as the heavy store loading configuration.

At NLR, a computational grid suitable for the solution of the Euler flow field equations is available for this configuration. However, for LCO simulations a Navier-Stokes flow model is required because shock-induced flow separation is present in the flow field. Unfortunately, a computational grid suitable for the solution of the Navier-Stokes flow field equations will be extremely complex to generate and unmanageable during the execution of the computations. Therefore, simplifications of the geometry have been sought and carried out.

The main assumption underlying the present LCO investigations is the finding in previous work, e.g. Refs. [12–14], that the origin of LCO for the heavily-loaded F-16 is the occurrence of shock-induced flow separations at the outer part of the wing. This observation has been used as the basis to judge whether geometry simplification is allowed. The simplifications have also been validated using steady and unsteady measurement data. The underwing stores and the wing tip missiles will not be included in the aerodynamic computations. However, the wing tip launcher has been maintained in the model. Also the tail section of the aircraft has been omitted. The reduction of the geometrical complexity is also shown in Figure 19.

The next step in the computational procedure is the mapping of the mode shapes from the nodes on the structural grid to the nodes on the aerodynamic grid. In the structural dynamics module of the CAS system, all components of the configuration are always taken into account in contrast to the aerodynamics module. The volume spline method is applied to interpolate the mode shapes. Examples of the mapped mode shapes are shown in Figure 20 that presents the first four flexible anti-symmetrical mode shapes of the F-16 heavy store configuration. In total 10 symmetrical and 10 anti-symmetrical mode shapes have been used in the simulation. For the present investigation, a very small structural damping has been used throughout the simulations.

Dynamic aeroelastic simulations have been carried out for a flight speed that corresponds to $M_\infty = 0.90$ at an altitude of 10,000 ft (usually called FL100) and an angle of attack of 7 degree and zero angle of side slip. This condition has been selected in order to correspond to the condition that has been used in a previous study of Meijer [12]. The simulations have been started from a steady flow field condition and with a rigid structure. Through inclusion of the symmetrical mode shapes in the simulation, the static deformation of the structure has also been obtained as part of the solution. Thus, in the present simulations, the absolute deformations have been computed instead of deformations that are taken with regard to the static deformation state. Initial conditions have been specified for all anti-symmetrical mode shapes in the form of an initial generalised velocity.

Figure 21 shows a typical time history of the generalised coordinates for the symmetrical mode shapes during an LCO simulation based on application of the Navier-Stokes equations. The time traces feature oscillations around averaged values that correspond to static deformations. It is evident that the oscillations do not wash out. The amplitudes of the oscillations initially increase to a certain level and remain at those levels next. This is characteristic for the LCO phenomenon.

Figure 22 shows the time history of the generalised coordinates for the anti-symmetrical mode shapes during the same simulation. In contrast to the symmetrical mode responses, the deformations feature oscillations around the initial, undeformed state. These responses represent largely the dynamic deformations. Only the first two mode shapes, the first wing bending and torsion mode shape, feature oscillations that initially increase up to a certain level and remain at those levels next. The other mode shapes damp out. It can be concluded that the first and second mode are coupled by the aerodynamic forces and contribute to the instability. In the remaining part of the present report, the anti-symmetric mode shapes will mainly be presented because the investigation has been concentrated on the dynamic behaviour of the phenomena.

One of the characteristics of LCO that has been shown in the test case of the NACA-64A010 aerofoil and NLR 7301 aerofoil is that the LCO final state is invariant to the initial condition, see Figure 14, Figure 15, Figure 17 and Figure 18. This feature has also been investigated for the LCO of the F-16. For this purpose, two simulations have been carried out based on the Navier-Stokes equations. The first simulation is performed using a relatively small initial velocity, while the second one uses a relatively large initial velocity. Figures 23 and 24 show the first anti-symmetrical bending and torsion mode shapes for small and large initial velocity, respectively. The final LCO amplitudes for the two simulations are the same although the paths to reach this state are different. The first part of the time history for the simulation with small initial condition shows a typical response of in case of flutter, i.e. an exponentially growing amplitude of the oscillations. After a long period of oscillations with increasing amplitude, the growth of the amplitude decreases until a stable LCO is obtained. From the point of view of the numerical approach, this type of simulation is not preferable because it requires a very long simulation time. The case with large initial velocity, on the other hand, does not feature long transient responses and reaches quickly the LCO condition. For an LCO investigation using numerical tools, this latter type of response is preferable.

The dependency of the LCO amplitude on the dynamic pressure has been shown in the test case of the NACA-64A010 aerofoil and has also been observed in the flight test of the RNLAF. To check whether the present CAS method captures this dependency properly, a simulation has been carried out at the same Mach number $M_\infty = 0.90$ but at an altitude 1,000 ft lower than the previous simulation, i.e. at FL90. Comparison of the responses of the anti-symmetrical first bending and torsion mode shapes at FL90 with those from the previous simulation at FL100 is shown in Figures 25 and 26. The figures show that the amplitude of the LCO increases with increasing dynamic pressure.

Finally, the analysis of the results is presented. The surface pressure distributions during one cycle of LCO are shown in Figure 27. The time step size applied in the simulation is 6.33 milliseconds. During the occurrence of LCO, the small surface deformations cause significant changes to the surface pressure distribution. The surface deformation has been rendered in this figure with its real magnitude. To be able to see the deformation more clearly, the surface deformation during one cycle of LCO is plotted at a magnitude of 7 times its real deformation in Figure 28. This figure confirms the observation from the time histories of the generalised coordinates that the LCO consists of a coupled anti-symmetrical bending and torsion mode. The frequency content of the time trace has been analysed using Fourier transformation. Figure 29 shows the magnitude of the Fourier components of the deformation at a measurement point in the foremost part of the starboard wing tip missile launcher. A comparison has been made with flight test data of the RNLAF. The frequency spectrum features a very dominant component at about 5.5 Hz. Very good correspondence is found between the result from the numerical simulation and from the flight test. The acceleration at a certain point is determined by application of a finite difference scheme to the values of the velocity that are computed during the simulation. The acceleration at a measurement point in the foremost part of the starboard missile launcher is presented in Figure 30. The amplitude of the oscillation is larger than the amplitude obtained from the flight test. Most probably, this is due to the very small value of structural damping used in the simulation. It is known from previous research that an increase of the structural damping will reduce the amplitude of the LCO. More detailed and systematic study of the structural damping will be carried out in future research. In any case, the present CAS method yields the correct tendency with respect to the acceleration. A summary of the main frequency spectrum and acceleration data is presented in Table 4.

parameter	simulation	flight test
main frequency in the response	5.46 Hz	5.5 Hz
acceleration amplitude	$\approx$ 6 g	$\approx$ 2 g

Table 4: Summary of the LCO simulation of the F-16 in heavy store configuration at $M_\infty = 0.9$, $\alpha = 7.0$ degree and altitude FL100

Summarising the previous discussion, it may be concluded that the results of the present investigation inspire confidence with respect to the validity of the method.

4 Concluding remarks

In this paper, the description and results of the computational aeroelastic simulation CAS system developed at NLR in the past years are presented.

Dynamic aeroelastic simulations have been described for configurations ranging from a two-dimensional aerofoil to the F-16 aircraft undergoing LCO. Based on the results of the simulations, the following conclusions can be drawn:

- The computational procedures that have been selected and applied in the present CAS system have been found to be robust and efficient.
- The LCO occurring at the F-16 aircraft in heavy-store loading configuration at a moderate angle of attack has been successfully simulated. The frequency of the LCO obtained from the simulation corresponds well to the frequency observed during flight tests. The amplitude of the oscillations, however, has been found too high in the computations.

- For the case of NLR 7301 aerofoil, the present results confirm the finding published in the literature that the numerically computed amplitude of LCO is far larger than that observed in the experiment. However, the frequency of the LCO and the mode of the LCO are in a good agreement with the experiment.
- In all of the LCO cases investigated in the present work, i.e. the inviscid LCO of NACA 64A010, the DLR case of NLR 7301 and the F-16 heavy store configuration, the final LCO state is invariant to the initial condition.
- The amplitude of the LCO depends on the free-stream dynamic pressure as shown in the case of NACA 64A010 and F-16 heavy store configuration.
- Reducing the required length of simulation to investigate LCO can be done by applying a relatively large disturbance for the initial condition.
- Further investigation on LCO phenomenon and non-linear aeroelasticity in general, can now be carried out using the newly developed computational aeroelastic simulation method.

During the development and applications of the present CAS system, several issues have been identified that are recommended to be investigated in future research.

- The computed amplitude of LCO which are too large for the NLR 7301 case and for the F-16 heavy store case should be further investigated. In the case of NLR 7301 modelling of porous tunnel wall is one of the possible causes of discrepancy. For the F-16 case, the use of better values of structural damping should be investigated.
- As suggested in various publications, nonlinearity in the structural dynamics of fighter aircraft may play also an important role during an LCO process. Structural nonlinearity such as free-play and dry-damping should be investigated to obtain a comprehensive understanding of the tramsonic LCO phenomenon.

REFERENCES

[1] O.O. Bendiksen and K.A. Kousen. Transonic flutter analysis using the Euler equations. AIAA Paper 87-0911, AIAA, 1987.

[2] P.C. Chen, D. Sarhaddi, and D.D. Liu. Limit cycle oscillation studies of a fighter with external stores. AIAA Paper 98-1727, AIAA, 1998.

[3] D. Darracq, S. Toumit, S. Champagneux, and A. Corjon. Prediction of flutter boundary with a transonic aeroelastic solver. In *Proceedings of 1999 International Forum on Aeroelasticity and Structural Dynamics*, Williamsburg, 1999. CEAS/AIAA/ICASE/NASA Langley.

[4] J.W. Edwards, R.W. Bennett, W. Whitlow Jr., and D.A. Seidel. Time marching transonic flutter solutions including angle of attack effects. AIAA Paper 82-0685, AIAA, 1982.

[5] C. Farhat and M. Lesoinne. Fast staggered algorithms for the solution of three-dimensional nonlinear aeroelastic problems. In *Numerical Unsteady Aerodynamics and Aeroelastic Simulation*, AGARD Report R-822, pages 7–1$\sim$7–11, 1998.

[6] M.H.L. Hounjet and B.J.G. Eussen. Outline and application of the NLR aeroelastic simulation method. In *Proceedings of 19th Congress of ICAS*, pages 1418–1441, Anaheim, 1994. ICAS, also NLR-TP-94422, NLR, 1994.

[7] M.H.L. Hounjet, B.J.G. Eussen, and M. Soijer. Analysis of aeroelastic simulations by fitting time signals. In *Proceedings of 1997 CEAS International Forum on Aeroelasticity and Structural Dynamics*, volume 3, pages 131–141, Rome, 1997. Associazione Italiana di Aeronautica ed Astronautica, also NLR-TP-97281, NLR, 1997.

[8] M.H.L. Hounjet and J.J. Meijer. Evaluation of Elastomechanical and Aerodynamic Data Transfer Methods for Non-planar Configurations in Computational Aeroelastic Analysis. In *Proceedings of 1995 CEAS International Forum on Aeroelasticity and Structural Dynamics*, pages 11.1–11.24, Manchester, 1995. Royal Aeronautical Society, also NLR-TP-95690, NLR, 1995.

[9] K. Isogai. On the transonic dip mechanism of flutter of a sweptback wing. *AIAA Journal*, 17:793–795, 1979.

[10] J.C. Kok. Resolving the dependence on the freestream values for the k-omega turbulence model. NLR Report TP-99295, NLR, 1999.

[11] E.M. Lee-Rausch and J.T. Batina. Calculation of AGARD wing 445.6 flutter using Navier-Stokes aerodynamics. AIAA Paper 93-3476-CP, AIAA, 1993.

[12] J.J. Meijer. Determination of transonic unsteady aerodynamics loads to predict the aeroelastic stability of fighter aircraft. In *Proceedings of 1997 CEAS International Forum on Aeroelasticity and Structural Dynamics*, volume 2, pages 373–382, Rome, 1997. Associazione Italiana di Aeronautica ed Astronautica, also NLR-TP-97304, NLR, 1997.

[13] J.J. Meijer and A.M. Cunningham Jr. Outline and applications of a semi-empirical method for predicting transonic limit cycle oscillation characteristics of fighter aircraft. In *Proceedings of 1995 CEAS International Forum on Aeroelasticity and Structural Dynamics*, pages 1–21, Manchester, 1995. Royal Aeronautical Society, also NLR-TP-95308, NLR, 1995.

[14] J.J. Meijer and A.M. Cunningham, Jr. A semi-empirical unsteady nonlinear aerodynamic model to predict transonic LCO characteristics of fighter aircraft. AIAA Paper 95-1340, AIAA, 1995, also NLR-TP-95183, NLR, 1995.

[15] M.P. Mignolet, D.D. Liu, and P.C. Chen. On the nonlinear structural damping mechanism of wing/store limit cycle oscillation. AIAA Paper 99-1459, AIAA, 1999.

[16] B.B. Prananta and M.H.L. Hounjet. Large time step aero-structural coupling procedures for aeroelastic simulation. In *Proceedings of 1997 CEAS International Forum on Aeroelasticity and Structural Dynamics*, volume 2, pages 63–71, Rome, 1997. Associazione Italiana di Aeronautica ed Astronautica, also NLR-TP-97619, NLR, 1997.

[17] B.B. Prananta and M.H.L. Hounjet. Large time step aero-structural coupling procedures for aeroelastic simulation. Report NLR-TP-97619, NLR, 1997.

[18] B.B. Prananta, M.H.L. Hounjet, and R.J. Zwaan. Two-dimensional transonic aeroelastic analysis using Thin-Layer Navier-Stokes method. *Journal of Fluids and Structures*, 12: 655–676, 1998.

[19] B.B. Prananta, I W. Tjatra, S.P. Spekreijse, J.C. Kok, and J.J. Meijer. Static aeroelastic simulation of military aircraft configuration in transonic flow. In *Proceedings of International Forum on Aeroelasticity and Structural Dynamics, June 4-6 2001*. AIAE, also NLR-TP-2001-346, NLR, 2001.

[20] G. Schewe, A. Knipfer, H. Mai, and G. Dietz. Experimental and numerical investigation dynamic loads of fighter-type aircraft. IB 232-2002 J 01, DLR, 2002. translated from Deutsch by W. King III.

[21] E.F. Sheta, V.J. Harrand and. D.E. Thompson, and T.W. Strganac. Computational and experimental investigation of limit cycle oscillation of nonlinear aero-elastic system. *Journal of Aircraft*, 39(1):133–141, 2002.

[22] S.P. Spekreijse, B.B. Prananta, and J.C. Kok. A simple, robust and fast algorithm to compute deformations of multi-block structured grids. NLR Report TP-2002-105, NLR, 2002.

[23] J.L. Steger and H.E. Bailey. Calculation of transonic airleron buzz. AIAA Paper 79-0134, AIAA, 1979.

[24] L. Tang, R.E. Bartels, P.C. Chen, and D.D. Liu. Numerical investigation of transonic limit cycle oscillations of a two-dimensional supercritical wing. *Journal of Fluids and Structures*, 17:29–41, 2003.

[25] P.A. van Gelder, J.J. Meijer, J. van Muijden, B.B. Prananta, and J.H. van Tongeren. F-16 wing loads under heavy-load condition. In *Proceedings of 2003 CEAS International Forum on Aeroelasticity and Structural Dynamics*, Amsterdam, 2003. NVvL, also NLR-TP-2003-533, NLR, 2003.

[26] S. Weber, K.D. Jones, J.A. Ekaterinaris, and M.F. Platzer. Transonic flutter computations for the NLR 7301 supercritical wing. *Aerospace Science and Technology*, 5:293–304, 2001.

[27] E.C. Yates Jr. AGARD standard aeroelastic configurations for dynamic reponse, I-wing 445.6. Report R-765, AGARD, 1988.

[28] R.J. Zwaan. Aeroelasticity of aircraft. Lecture Note D-44, Delft University of Technology, 1990.

FIGURES

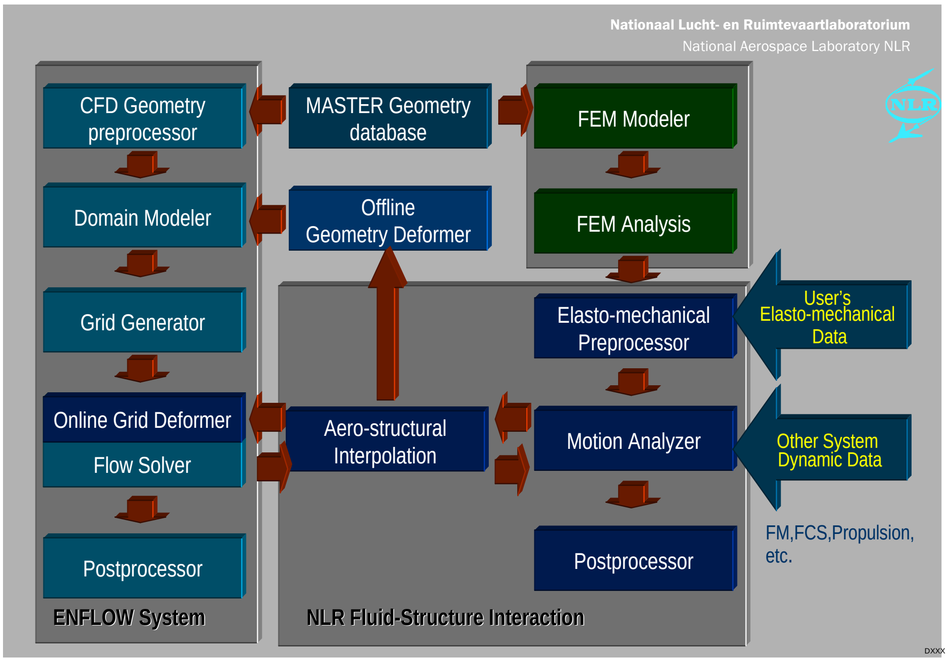

Figure 1: Schematic diagram of the present CAS system for computational aeroelastic simulation based on the NLR ENFLOW CFD system

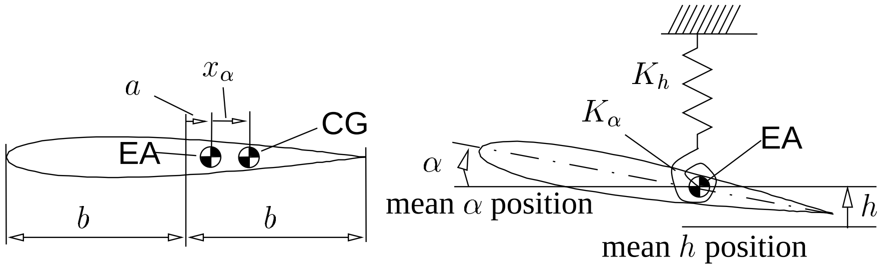

Figure 2: Characteristic wing section and the main parameters used in the mathematical model of two-dimensional aeroelastic computations

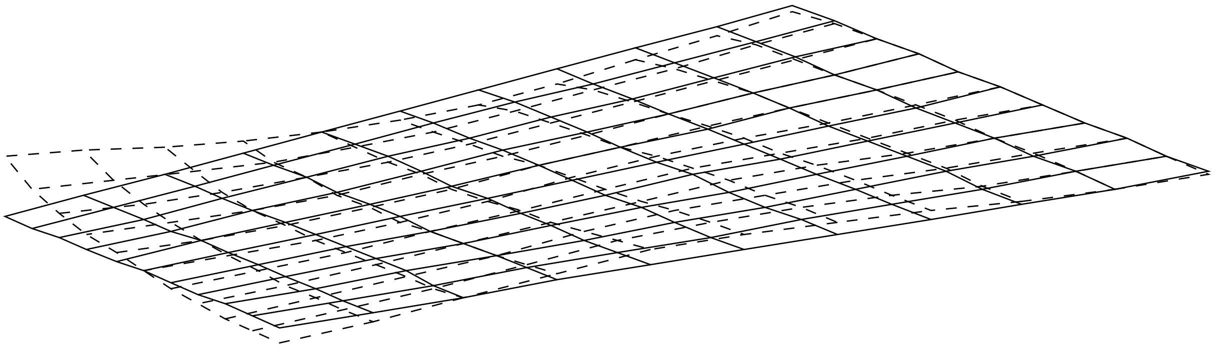

Figure 3: Finite element model of the AGARD 445.6 wing consisting of CQUAD4 shell elements; the dashed line shows the fourth flexible mode shape

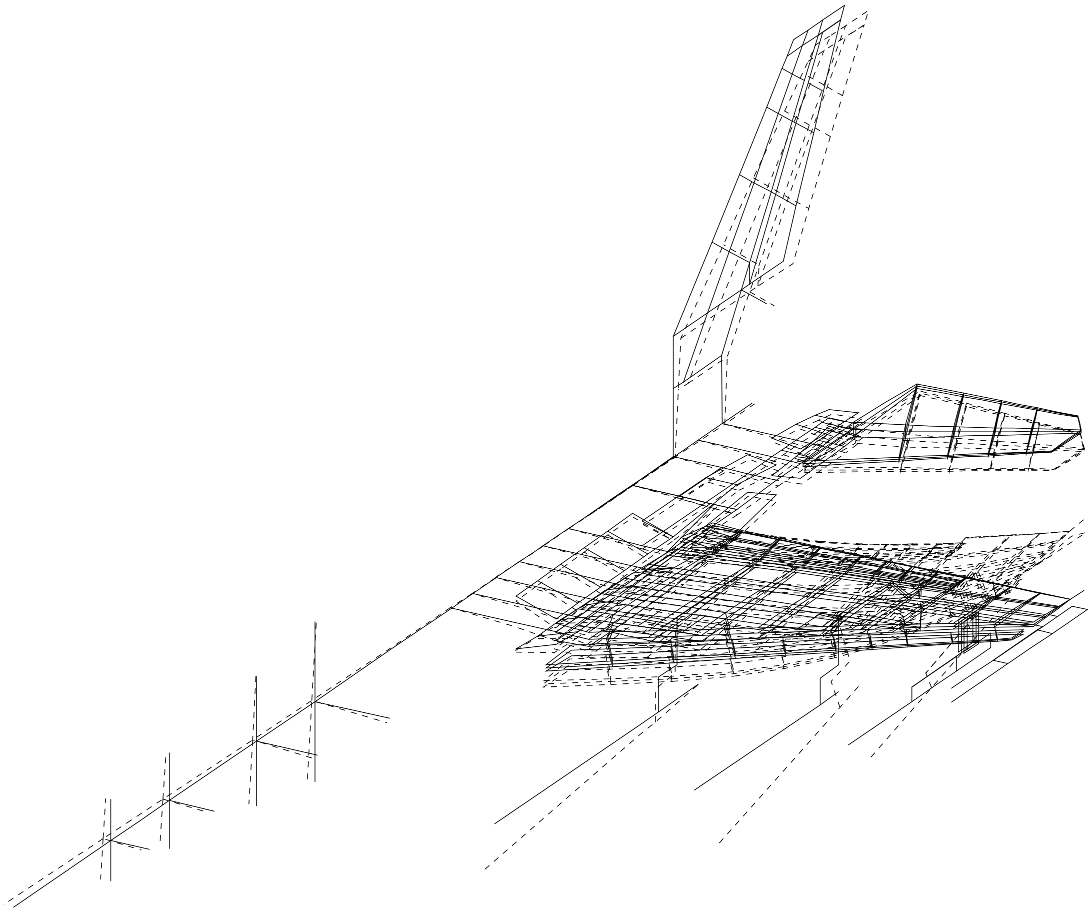

Figure 4: Finite element model of the F-16 aircraft in heavy store configuration consisting of CBEAM beam, CBAR bar and QUAD4 shell elements; the dashed line shows the first symmetrical flexible mode shape

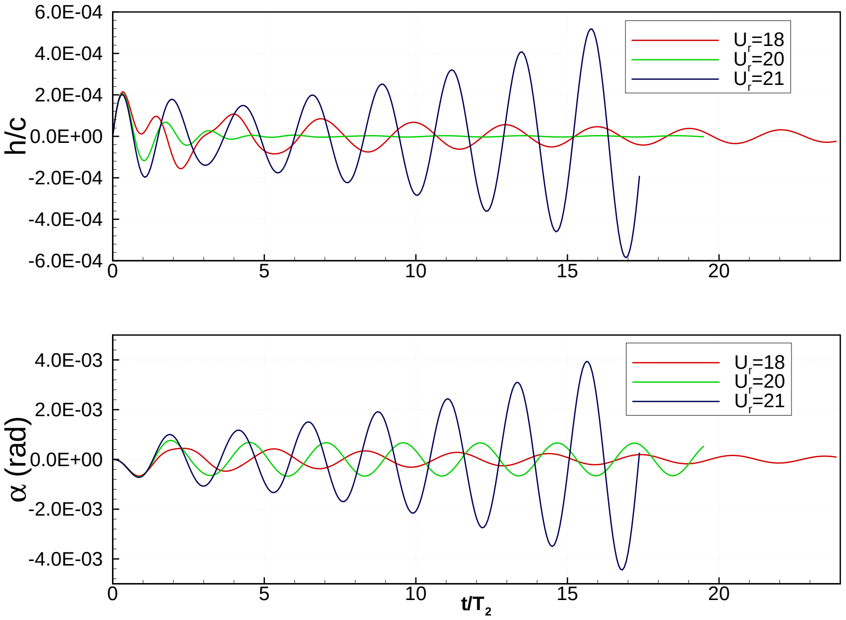

Figure 5: Pitching and plunging responses (exact solutions) of a flat plate for several reduced velocities; $M_\infty = 0$, $\mu = 100$, $e = -0.50$

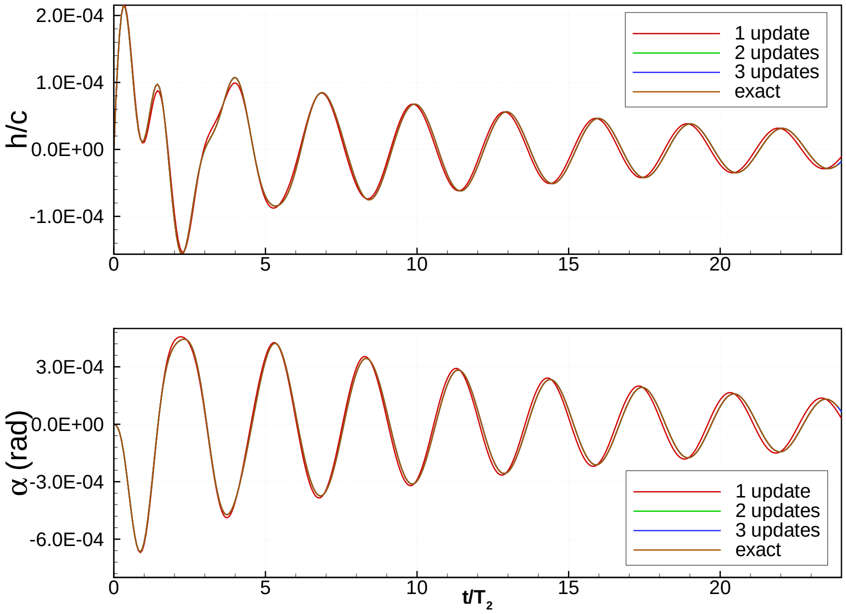

Figure 6: Pitching and plunging responses of a flat plate computed using the exact method and using the present CAS method for different numbers of structural updates in the fluid/structure coupling procedure; $M_\infty = 0$, $\mu = 100$, $e = -0.50$, $U_\mathrm{R} = 18$

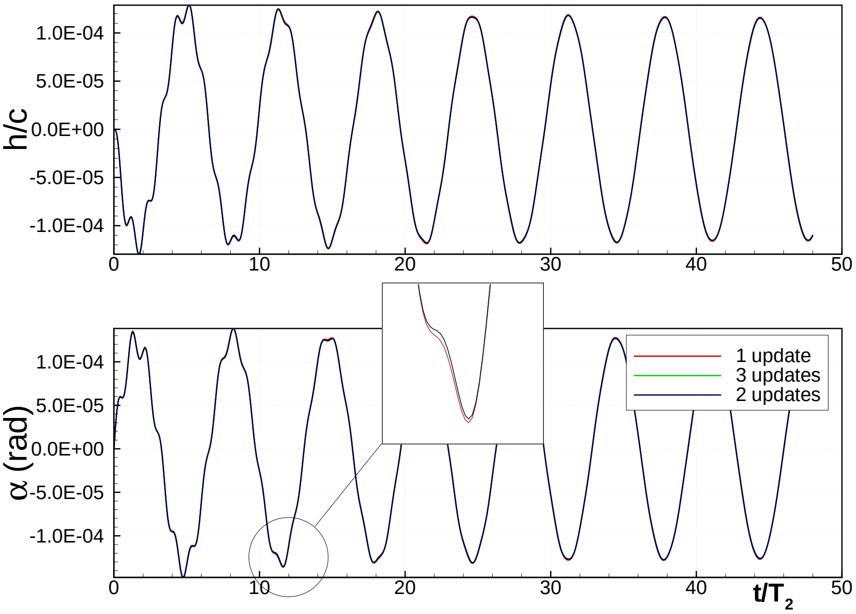

Figure 7: Pitching and plunging responses of the NACA 64A010 aerofoil computed using the present CAS method for different numbers of structural updates in the fluid/structure coupling procedure; $M_\infty = 0.85$, $\mu = 60$, $e = -0.50$, $U_\mathrm{R} = 4.26$, Euler flow model

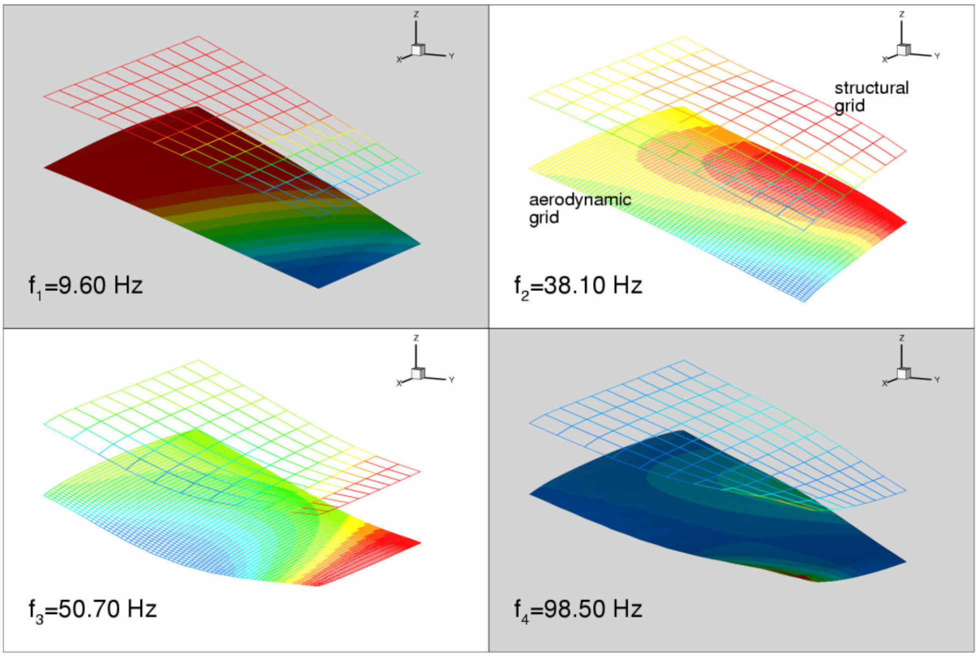

Figure 8: First four mode shapes of the AGARD 445.6 wing in the nodes of the structural grid and the mapping to the aerodynamic grid

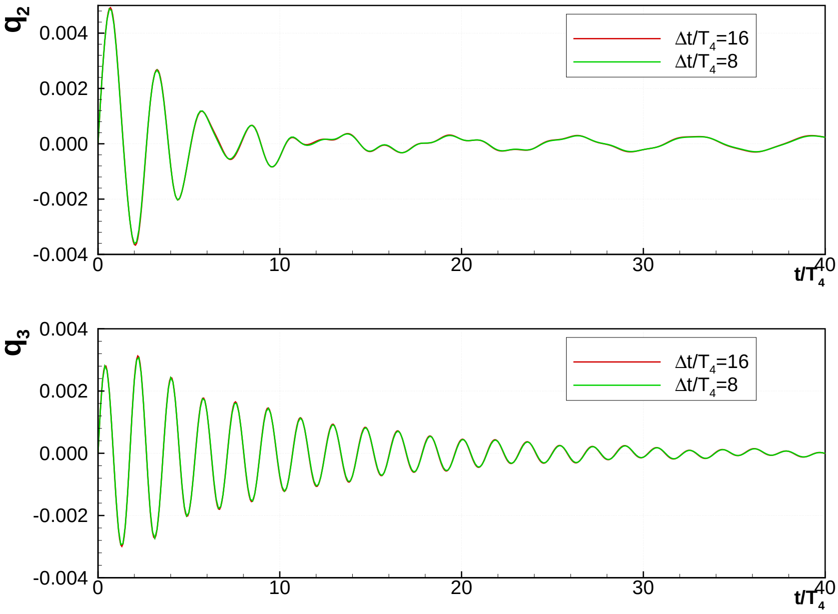

Figure 9: Time history of the generalised coordinates of the second and third mode shapes of the AGARD 445.6 wing using two time step sizes; $M_\infty = 0.96$, $V^* = 0.2$, Euler flow model

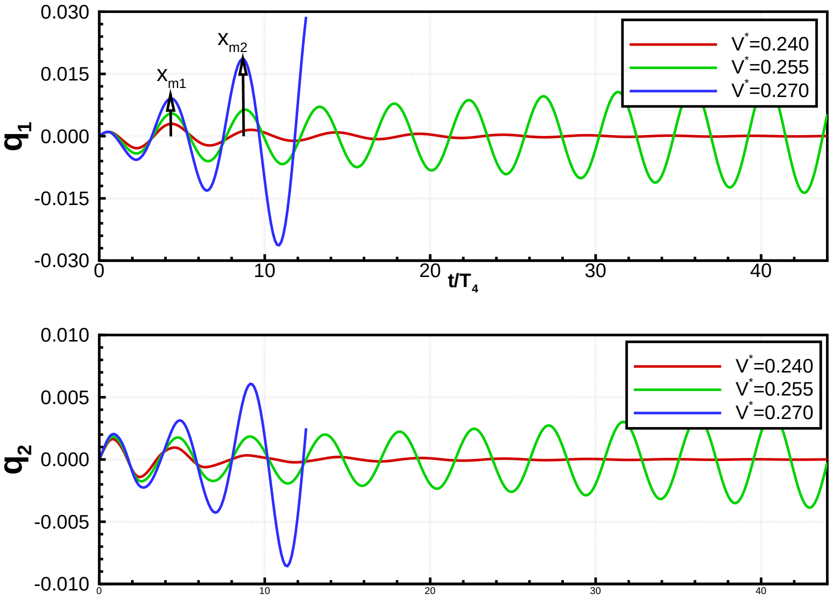

Figure 10: Time history of the generalised coordinates of the first and second mode shapes of the AGARD 445.6 wing for three speed indices ($V^* = 0.240, 0.255$ and 0.270); $M_\infty = 0.499$, Euler flow model

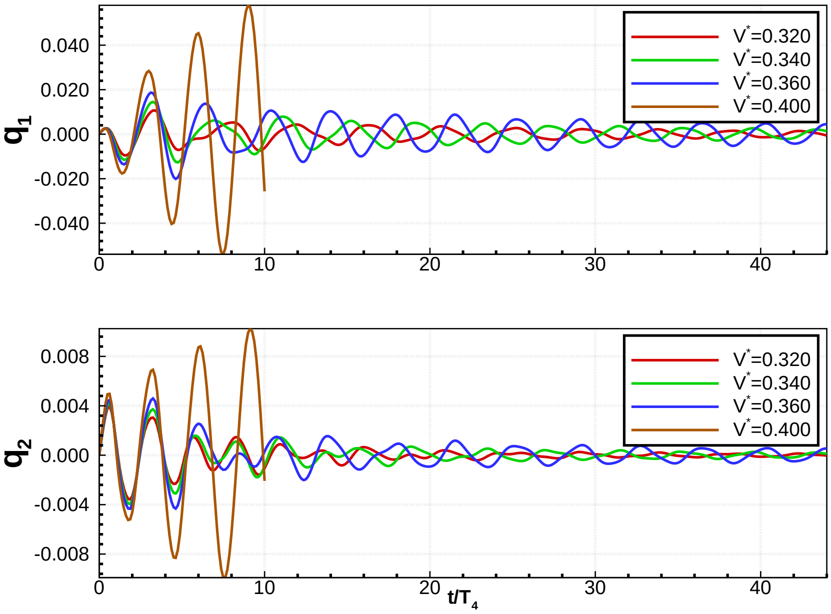

Figure 11: Time history of the generalised coordinates of the first and second mode shapes of the AGARD 445.6 wing for four speed indices $V^* = 0.32, 0.34, 0.36$ and 0.40, $M_\infty = 1.141$, Euler flow model

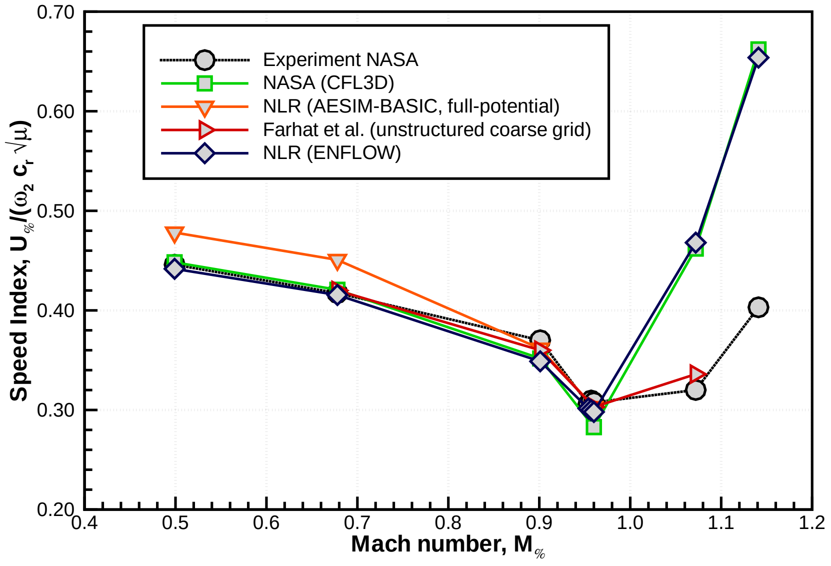

Figure 12: Flutter boundaries of the AGARD 445.6 wing predicted using the present CAS method (Euler flow model) and other computational methods and experimental data

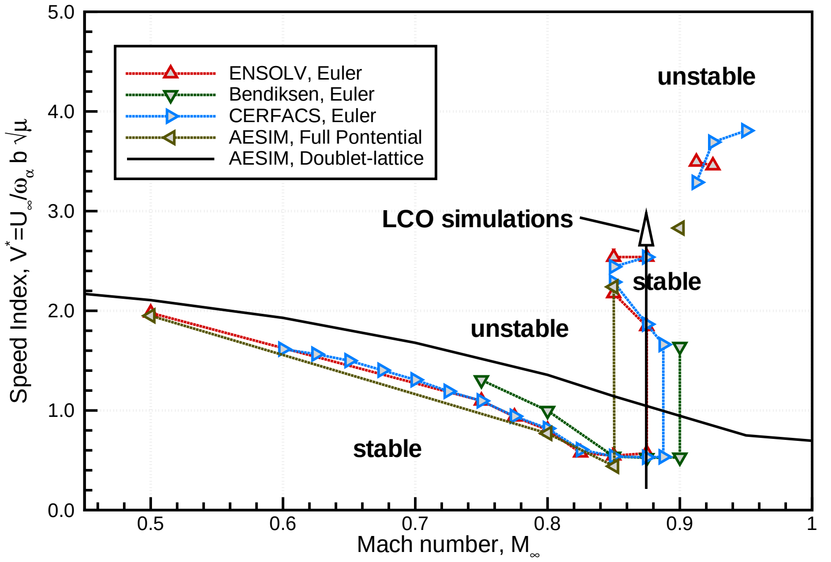

Figure 13: Flutter boundaries of the NACA 64A010 aerofoil computed using the present CAS method (Euler flow model) and other computational methods

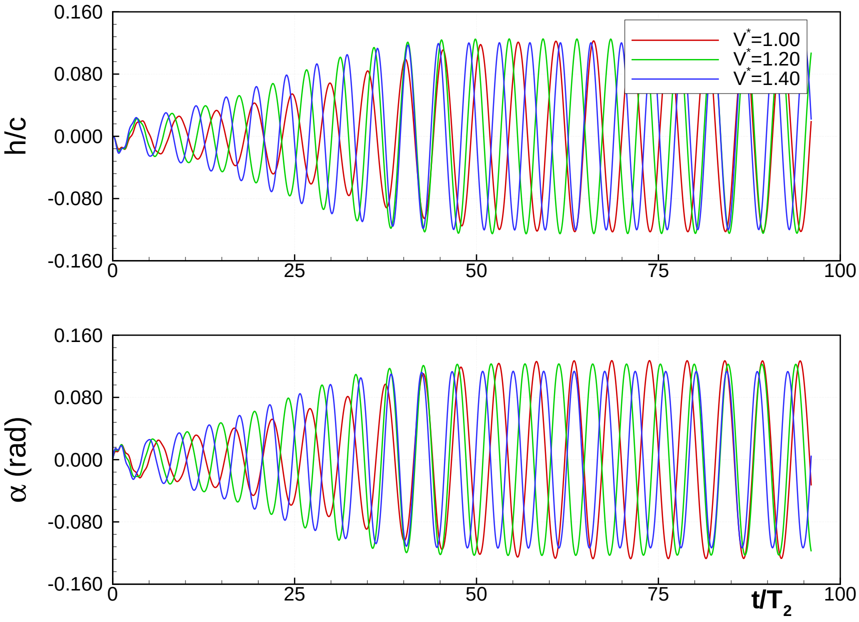

Figure 14: Time history of the pitching and plunging responses of the NACA 64A010 aerofoil for three speed indices ($V^* = 1.0, 1.2$ and 1.4); $M_\infty = 0.875$, Euler flow model

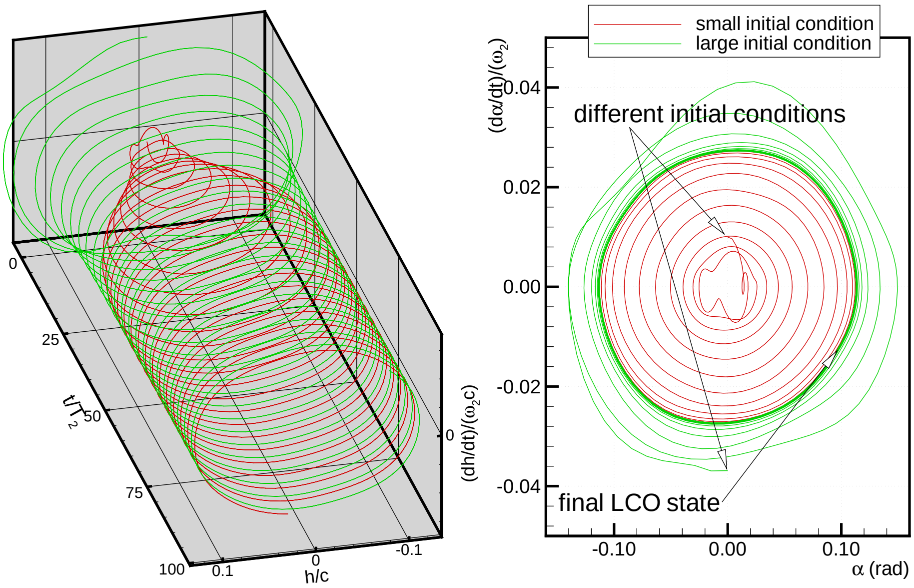

Figure 15: Pitching motion (phase plane plot) of the NACA 64A010 aerofoil at speed index $V^* = 0.60$ for two initial conditions; $M_\infty = 0.875$, Euler flow model

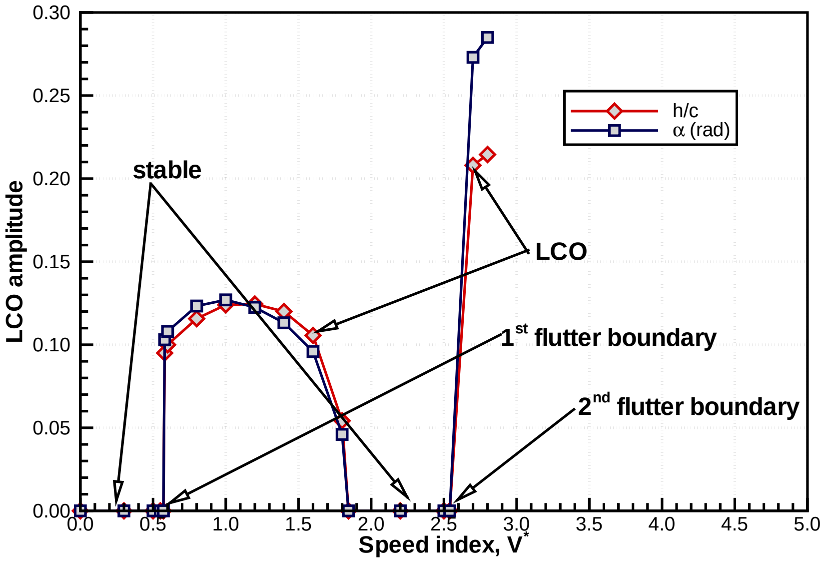

Figure 16: Dependency of the LCO amplitude on the speed index for the NACA 64A010 aerofoil; $M_\infty = 0.875$, Euler flow model

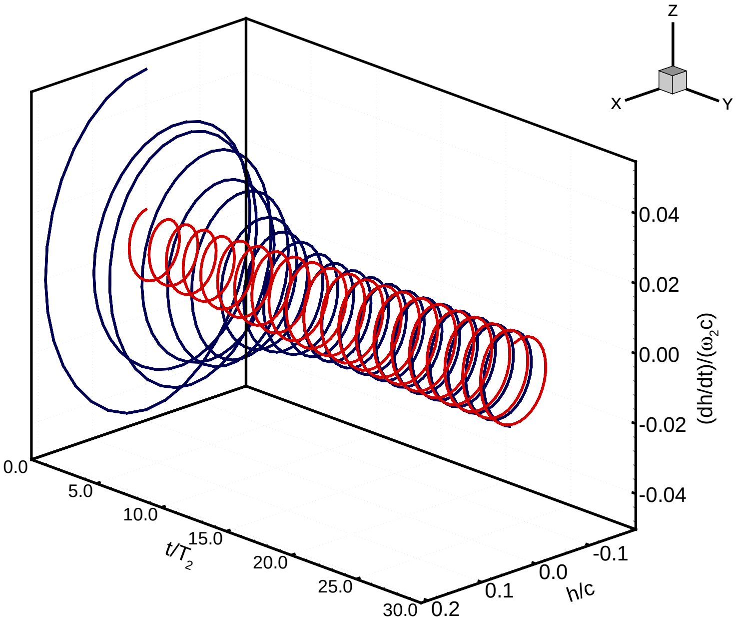

Figure 17: Time history of the plunging responses of the NLR 7301 aerofoil at MP77 condition of Ref. [20] for small and large disturbance initial conditions, $M_\infty = 0.754$, $\alpha = -0.15$, Reynolds-Averaged Navier-Stokes flow model

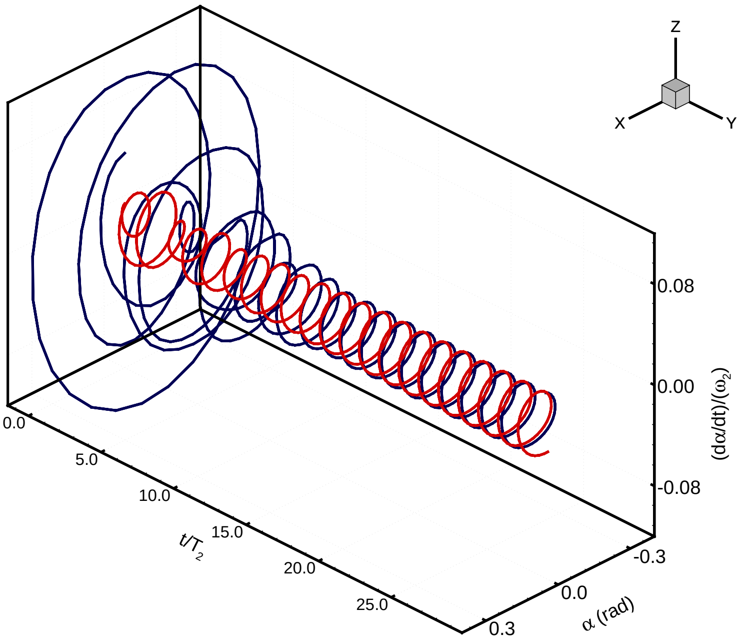

Figure 18: Time history of the pitching responses of the NLR 7301 aerofoil at MP77 condition of Ref. [20] for small and large disturbance initial conditions, $M_\infty = 0.754$, $\alpha = -0.15$, Reynolds-Averaged Navier-Stokes flow model

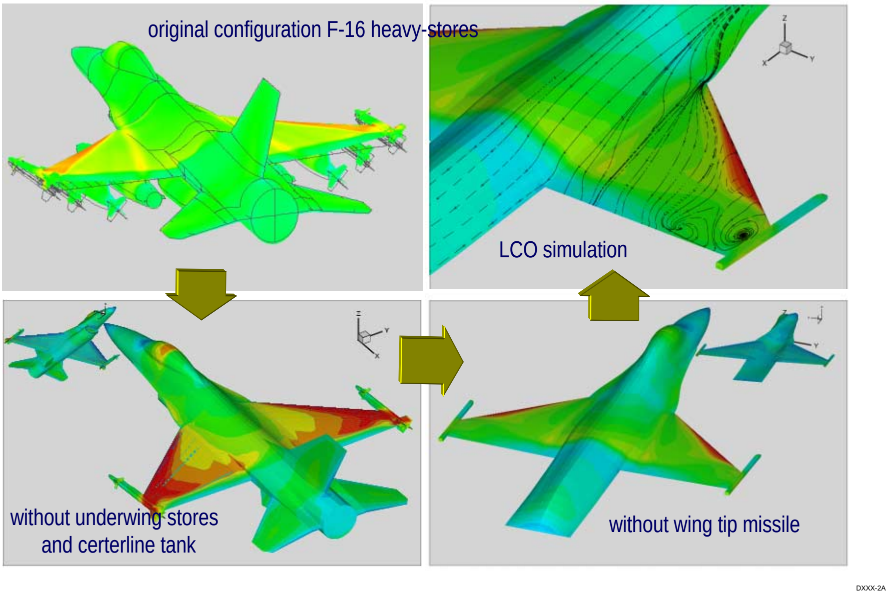

Figure 19: Reduction of the geometrical complexity of the F-16 heavy store configuration for the LCO simulation

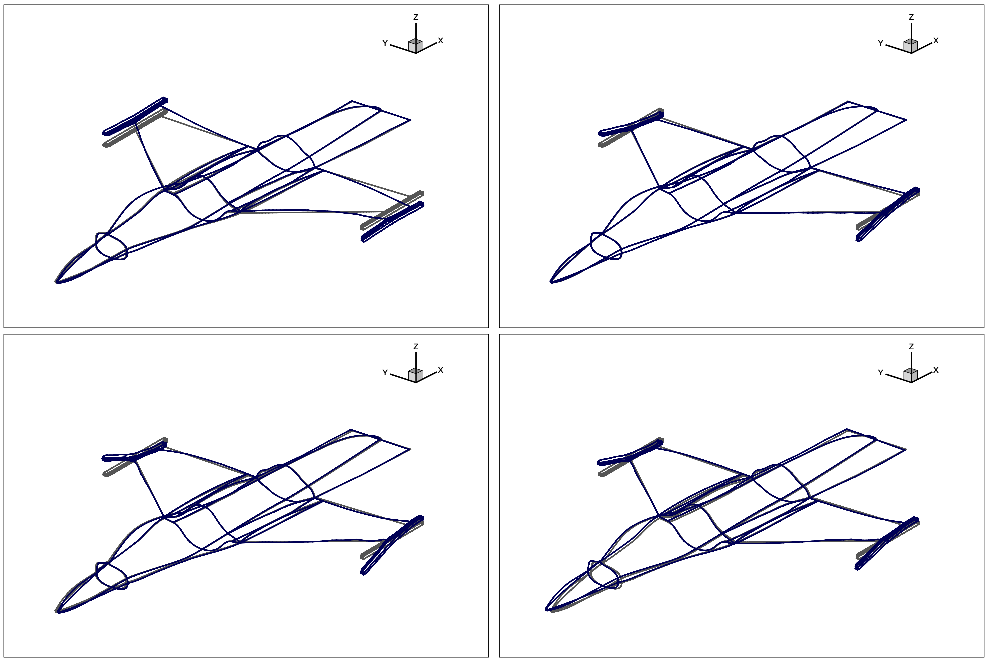

Figure 20: First four interpolated flexible anti-symmetrical mode shapes of the F-16 aircraft as applied in the LCO simulation

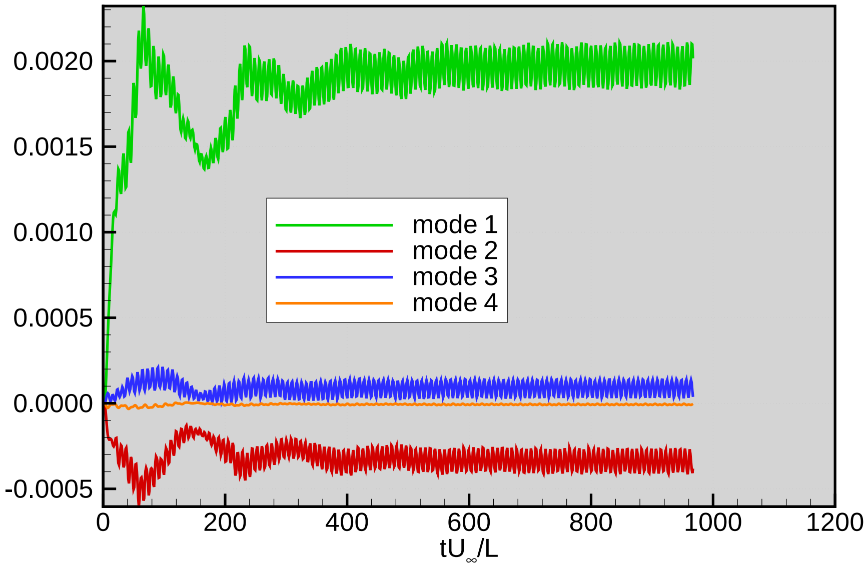

Figure 21: Time history of the generalised coordinates for the symmetrical modes of the F-16 aircraft during the LCO simulation; $M_\infty = 0.90$, $\alpha = 7$ degree, FL100, Reynolds-Averaged Navier-Stokes flow model

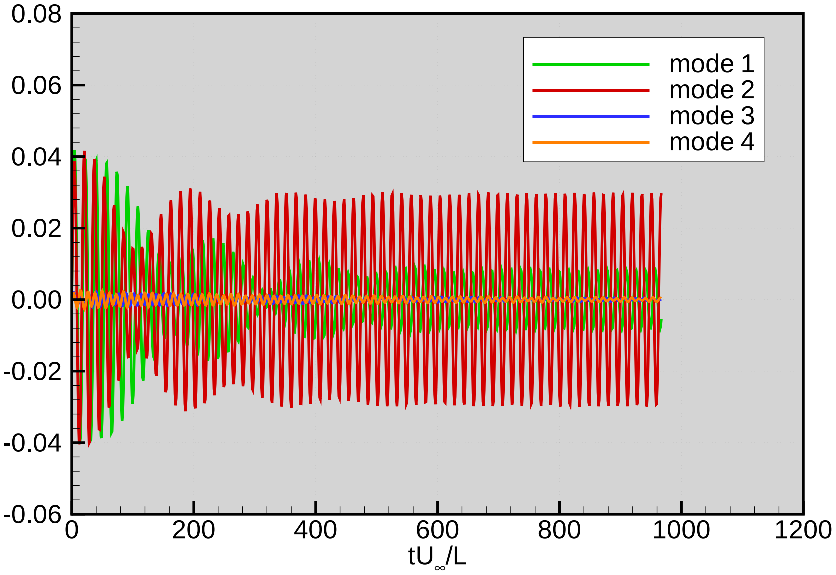

Figure 22: Time history of the generalised coordinates for the anti-symmetrical modes of the F-16 aircraft during the LCO simulation; $M_\infty = 0.90$, $\alpha = 7$ degree, FL100, Reynolds-Averaged Navier-Stokes flow model

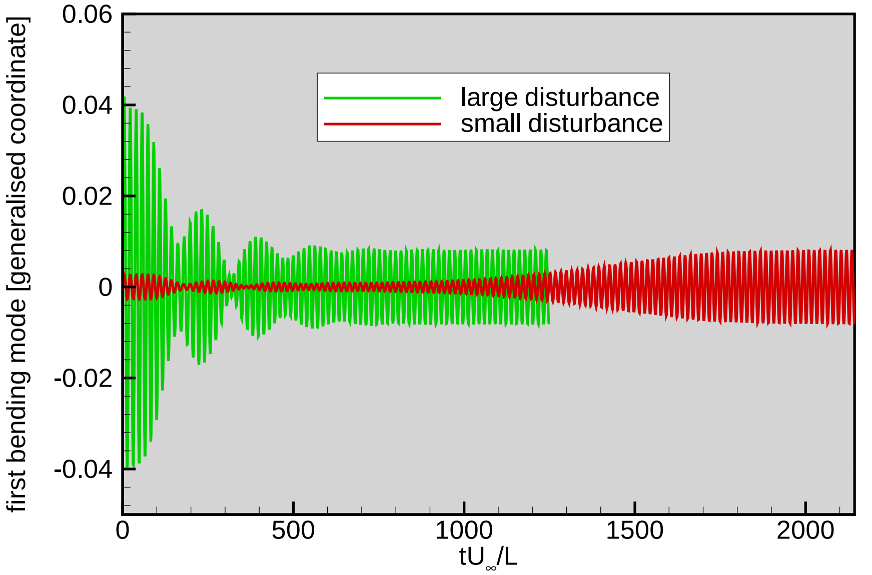

Figure 23: Time history of the generalised coordinates for the first anti-symmetrical bending mode of the F-16 aircraft for two initial velocities; $M_\infty = 0.90$, $\alpha = 7$ degree, FL100, Reynolds-Averaged Navier-Stokes flow model

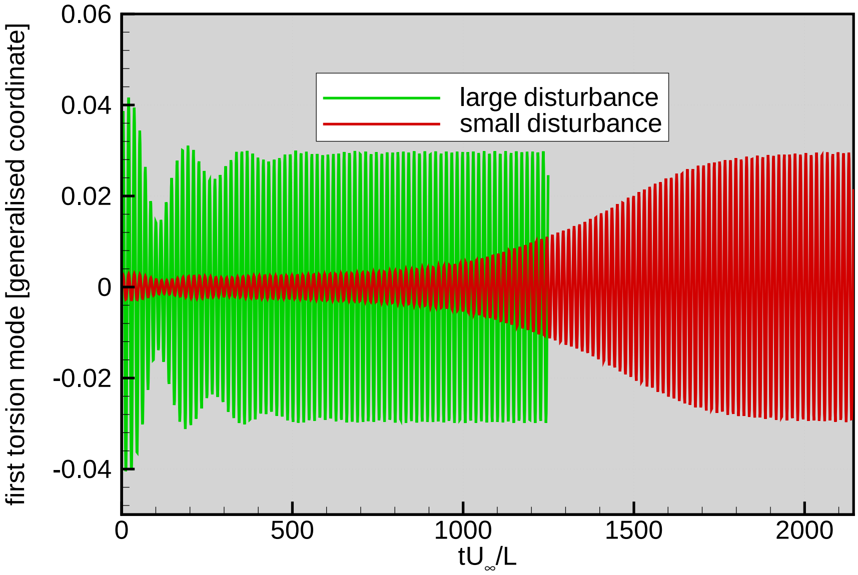

Figure 24: Time history of the generalised coordinates for the first anti-symmetrical torsion mode of the F-16 aircraft for two initial velocities; $M_\infty = 0.90$, $\alpha = 7$ degree, FL100, Reynolds-Averaged Navier-Stokes flow model

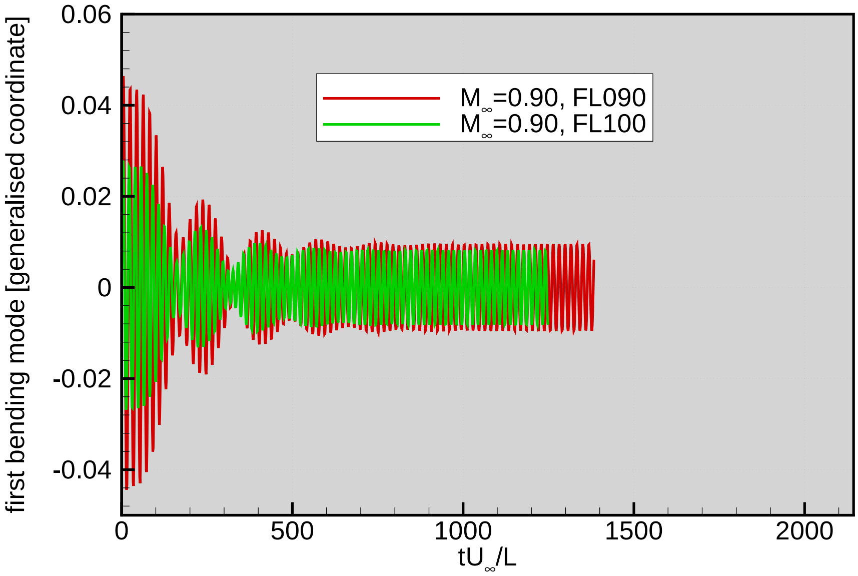

Figure 25: Time history of the generalised coordinates for the first anti-symmetrical bending mode shape of the F-16 aircraft for two altitudes; $M_\infty = 0.90$, $\alpha = 7$ degree, Reynolds-Averaged Navier-Stokes flow model

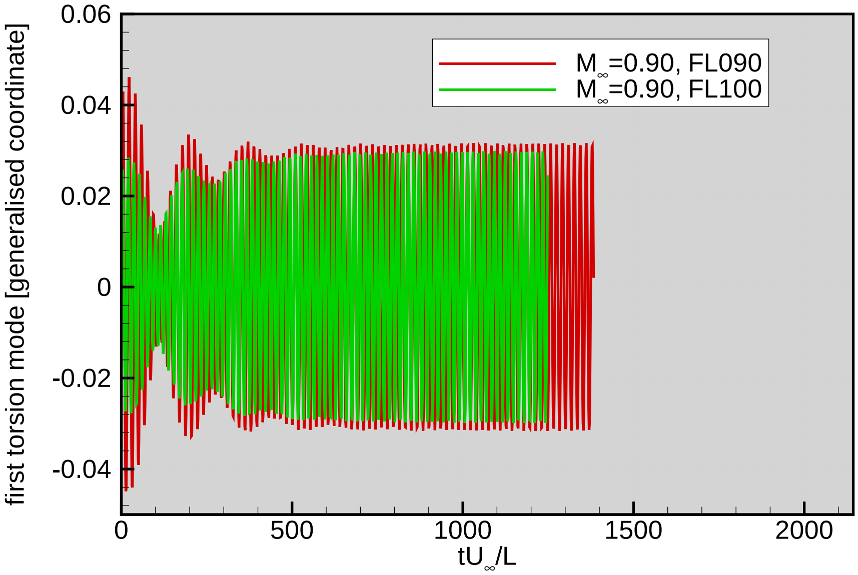

Figure 26: Time history of the generalised coordinates for the first anti-symmetrical torsion mode shape of the F-16 aircraft for two altitudes; $M_\infty = 0.90$, $\alpha = 7$ degree, Reynolds-Averaged Navier-Stokes flow model

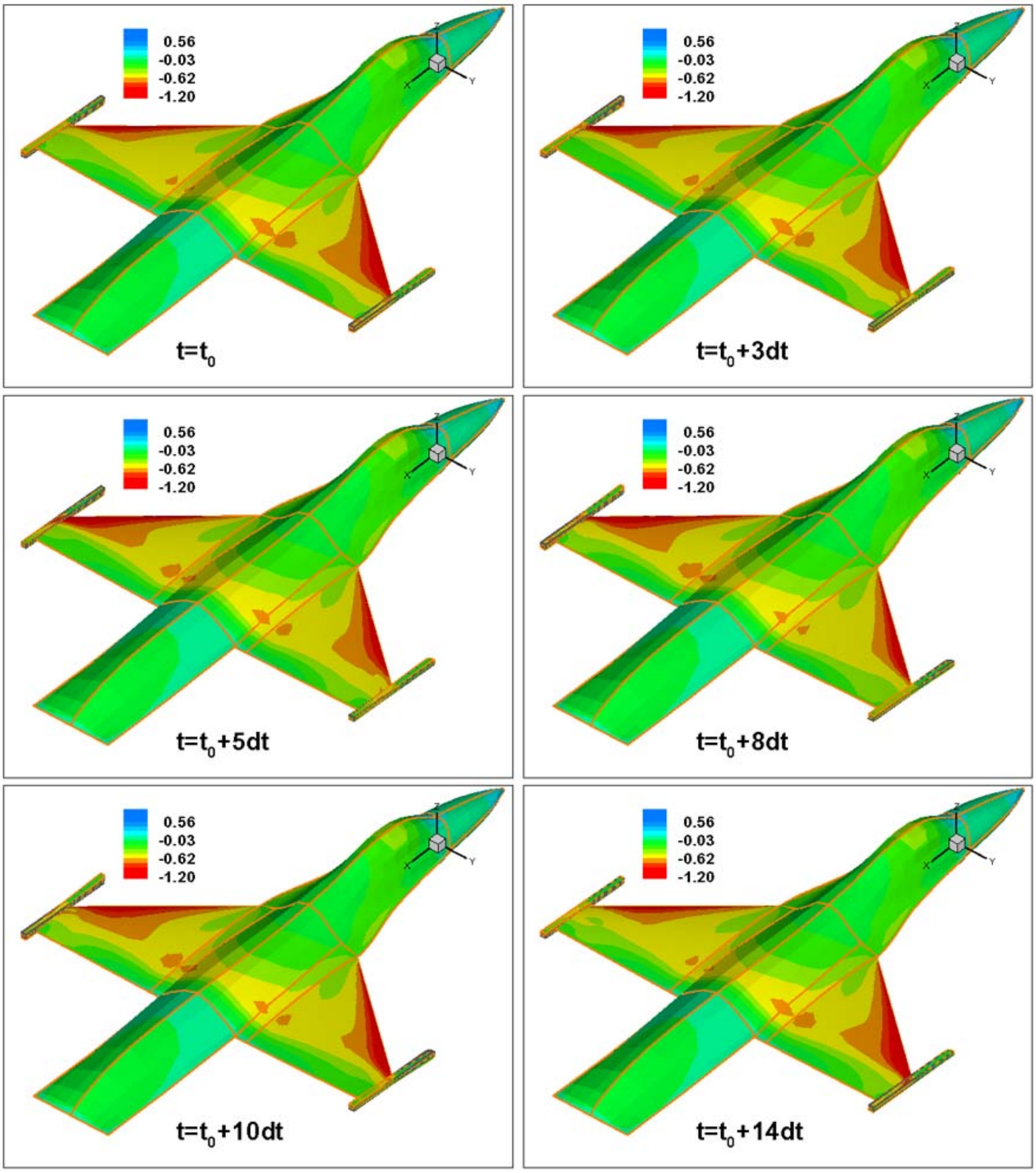

Figure 27: Surface pressure distributions during one cycle of LCO of the F-16 aircraft; $M_\infty = 0.90$, $\alpha = 7$ degree, FL100, Reynolds-Averaged Navier-Stokes flow model

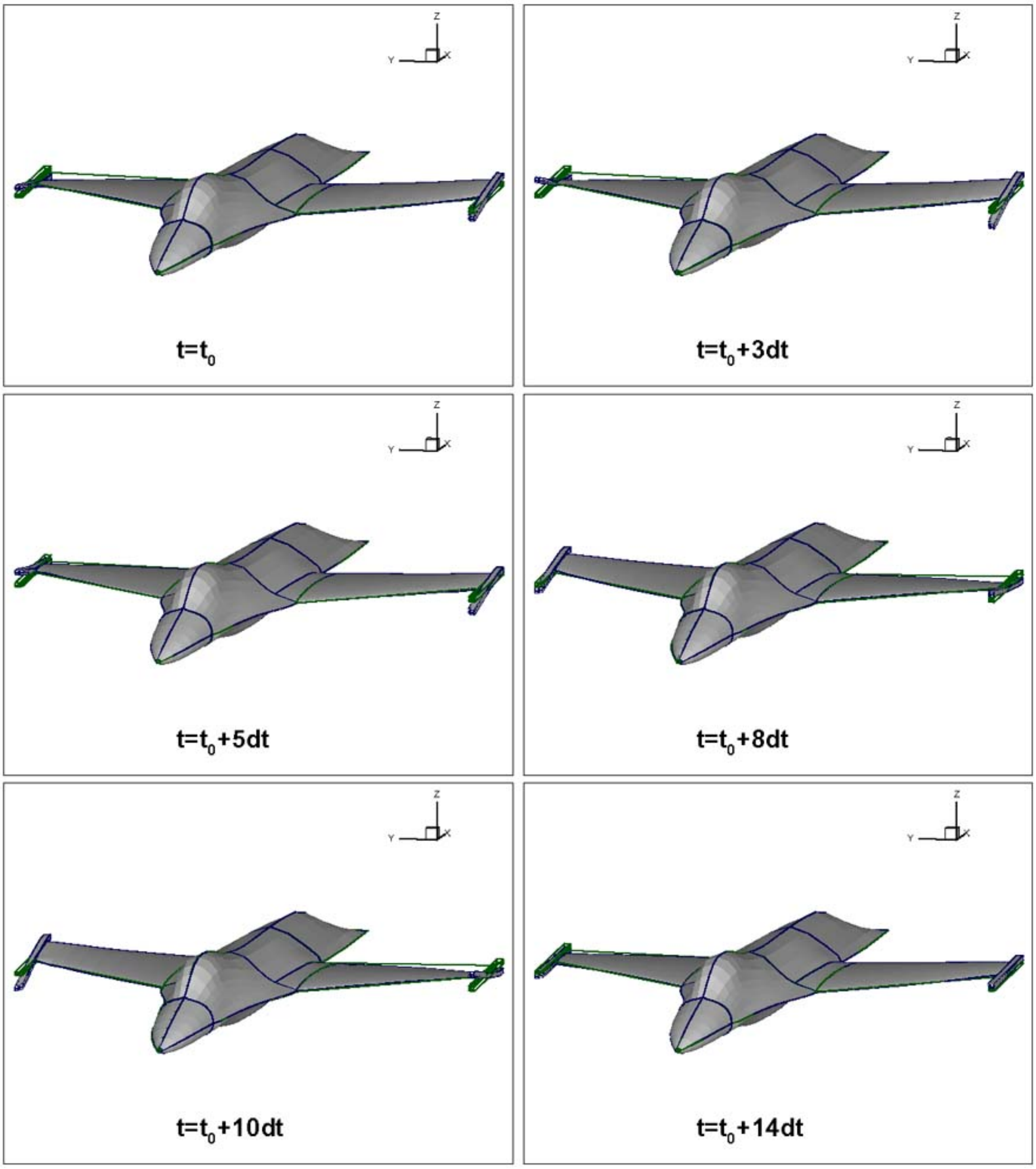

Figure 28: Surface deformations during one cycle of LCO of the F-16 aircraft plotted at a magnitude of 7 times its real deformation; $M_\infty = 0.90$, $\alpha = 7$ degree, FL100, Reynolds-Averaged Navier-Stokes flow model

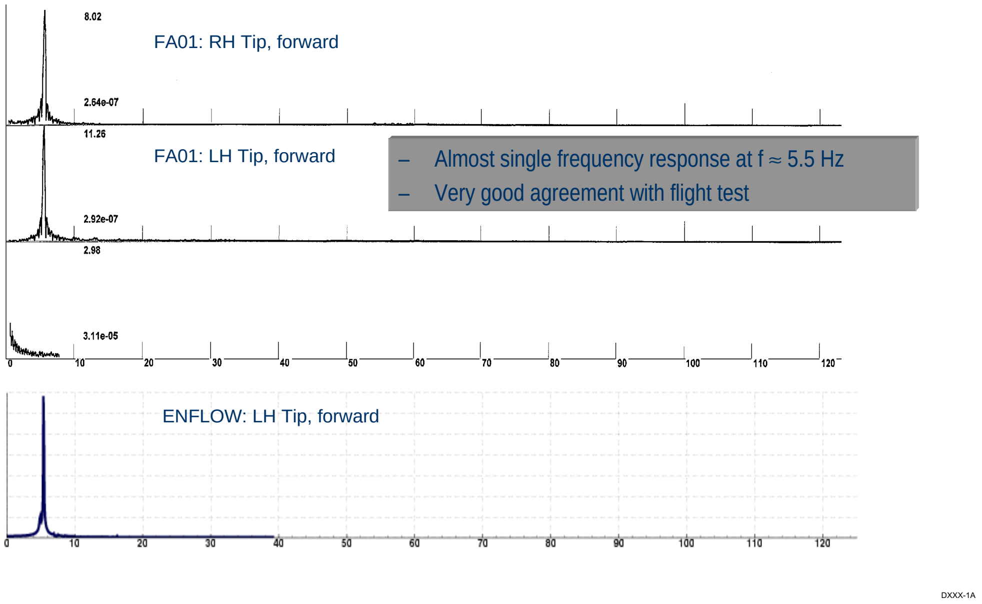

Figure 29: Frequency spectrum of the LCO responses of the F-16 aircraft at a measurement point in the foremost part of the starboard wing tip missile launcher computed using the present CAS method compared with the results of flight test; $M_\infty = 0.90$, $\alpha = 7$ degree, FL100, Reynolds-Averaged Navier-Stokes flow model

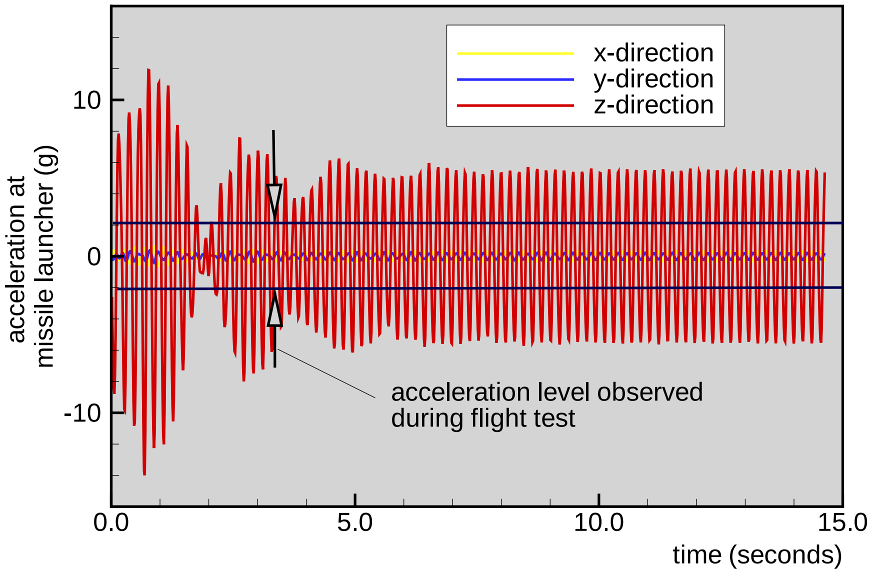

Figure 30: Acceleration during LCO of the F-16 aircraft at a measurement point in the foremost part of the starboard wing tip missile launcher computed using the present CAS method compared with the results of flight test; $M_\infty = 0.90$, $\alpha = 7$ degree, FL100, Reynolds-Averaged Navier-Stokes flow model

LIST OF SYMBOLS

b	half chord
$\boldsymbol{C}$	structural damping matrix
$\boldsymbol{C}_{\mathsf{A}}$	vector of aerodynamic force coefficients
C_L	lift coefficient
C_M	pitching moment coefficient
c_{R}	reference length
e	distance between elastic axis and aerodynamic centre
$\mathcal{F}$	convective flux of the Navier-Stokes equations
$\boldsymbol{F}_{\mathsf{srf}}$	surface force vector
$\boldsymbol{h}$	displacement vector
$\boldsymbol{K}$	stiffness matrix
L_{ref}	reference length
$\boldsymbol{M}$	mass matrix
M_∞	Mach number
m	generalized mass matrix, $\phi^T \boldsymbol{M} \phi$
m_i	i-th diagonal element of generalized mass matrix
m_{ref}	reference mass
$\boldsymbol{n}$	normal vector
Q	flow variables $[\rho, \rho u, \rho v, \rho w, \rho E]^T$, i.e. density, momentum, total energy
Q_i	i-th element of generalized aerodynamic force vector
$\boldsymbol{q}$	vector of generalized coordinates
q_i	i-th generalized coordinate
R	residual of discretised Euler/Navier-Stokes equations
Re_∞	Reynolds number
$\mathcal{S}$	source terms of the Navier-Stokes equations
s	span
$\boldsymbol{u}$	velocity vector
U_{R}	reduced velocity, $u_\infty/(\omega_{\mathsf{ref}} L_{\mathsf{ref}})$
u_∞	free-stream velocity
V^*	speed index, $U_{\mathsf{R}}/\sqrt{\mu}$
$\boldsymbol{x}$	physical coordinate vector
v_{ref}	reference volume
α	angle of attack
ζ_i	viscous damping coefficient of i-th vibration mode
μ	mass ratio, $m_{\mathsf{ref}}/(\rho_\infty v_{\mathsf{ref}})$
ρ_∞	mass density of air
$\boldsymbol{\phi}$	matrix of vibration modes
$\boldsymbol{\phi}_i$	i-th vibration mode
ω_i	natural frequency of i-th vibration mode
ω_{ref}	reference frequency

Sub/Super-scripts

n	time level